

Integrated Approach for Post-fire Reinforced Concrete Structures Assessment

61 (4), pp. 677–699, 2017

<https://doi.org/10.3311/PPci.9830>

Creative Commons Attribution 

Flavio Stochino^{1*}, Fausto Mistretta¹, Paola Meloni²,
Gianfranco Carcangiu³

RESEARCH ARTICLE

Received 30 July 2016; Revised 13 February 2017; Accepted 22 February 2017

Abstract

In order to assess decay in the mechanical characteristics of fire-exposed Reinforced Concrete (RC), it is crucial to reconstruct the temperature time history and the evolution of strain and stress fields. In this paper, the state of the art of assessment methods is presented and applied to a real structure damaged by fire. It is a prestressed RC industrial warehouse located in the outskirts of the city of Cagliari (Italy). The collected data of several assessment methods are presented in order to produce the flowchart of an integrated approach for post-fire investigation. Among the various techniques, the authors highlight a thorough laser scanner geometric survey and destructive and non-destructive testing. In addition, the temperature distribution and its time history has been reconstructed by means of optical and Scanning Electron Microscopy, X-ray diffractometry, Thermogravimetric Differential Thermo-Analysis and calibrated Colorimetry.

Actually, refurbishment is needed, but the structure withstood the fire very well. Central columns displayed the most important damage, and several beams presented important deflections having lost the prestressing actions of the tendons.

Keywords

structural fire design, reinforced concrete, colorimetry, non-destructive testing, scanning electron microscopy, thermogravimetric differential thermo-analysis

1 Introduction

Assessing the extent and gravity of fire damage on reinforced concrete buildings is a crucial task in order to plan the rehabilitation or the demolition of their structures. Unfortunately, the fire resistance capacity of reinforced concrete is very difficult to assess, as concrete itself is a composite material with components characterized by different thermal properties, but also because moisture and porosity have a great influence on mechanical behaviour. In addition, steel reinforcements, unlike concrete, are very sensitive to the effects of high temperatures caused by fire.

These problems become more serious in the case of large and strategic buildings that perform an important service which cannot be interrupted without high social costs, see [1–5]. If the fire is followed or anticipated by an explosion, materials and structures are pushed to the limit. Indeed, the material constitutive laws are strongly modified by the joint effects of strain rate (see [6–8]) and of temperature (see [9–10]).

Several case studies on the effect of fire on real R.C. structure assessment are reported in the literature: Folic et al [11] present the data recorded on fire-damaged Novi Sad Open University; in [12] there is a detailed study of the serious fire in the Windsor Tower in Madrid. Majoros and Balázs [13] investigated the effects of fire attacks in three halls in Budapest.

Results obtained from real incidents (see also [14–16]) are important because knowledge coming from their analysis can be effectively applied to the design of new structures: an interesting example of this approach is reported in [17].

Considering the above-mentioned issues, it is very difficult to establish a list of tests or structural assessments which are always valid in case of fire. Nevertheless, it is possible to classify the most important structural fire damages in two main sets (see Figure 1):

- geometrical variations, due to thermal deformation, affecting a single element or a group of them. These variations can modify the load-bearing structural scheme and make the usually negligible second-order effects much more important;
- degradation of the mechanical characteristics of materials.

¹Dipartimento di Ingegneria Civile, Ambientale e Architettura

Facoltà di Ingegneria,

Università degli Studi di Cagliari

Cagliari, 09122, via Marengo 2, Italy

²Dipartimento di Ingegneria Meccanica, Chimica e dei Materiali,

Facoltà di Ingegneria,

Università degli Studi di Cagliari

Cagliari, 09122, via Marengo 2, Italy,

³Istituto di Scienze dell'Atmosfera e del Clima,

Consiglio Nazionale delle Ricerche,

Cagliari, 09042, Strada Pro.le Monserrato - Sestu Km. 0,700 Italy

*Corresponding author email: fstochino@gmail.com

These effects obviously have a direct impact on structural safety.

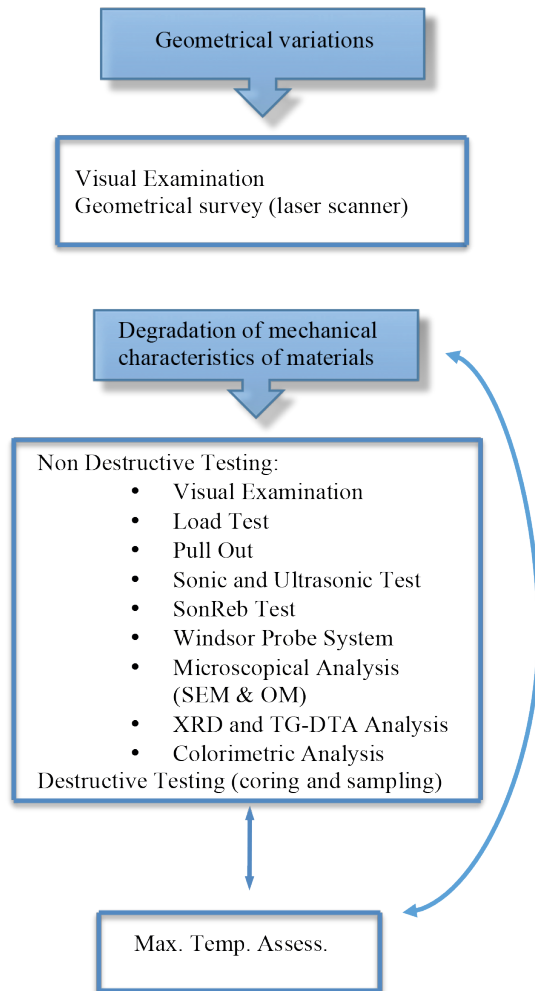


Fig. 1 Integrated approach flowchart for fire damages and corresponding assessment techniques.

While for the assessment of the first point a thorough geometrical survey of the damaged structure is generally sufficient (for example by means of the laser scanner, see [18–19]), in the second case it is crucial to reconstruct the temperature time history in order to determine the residual mechanical characteristics as proved in [20], where the authors studied compressive strength, splitting tensile strength and bending strength of concrete after high temperatures. In this paper, a set of experimental results describes the correlation between the compressive strength of concrete and the maximum temperature reached during the test. However, this is a very difficult task for real case study as back analysis starting from the damaged elements can be dramatically influenced by several unknown parameters regarding both the development of the fire and the initial structural characteristics.

As stated in [21], given the current state of assessment methods, experimental non-destructive and destructive techniques should be combined and refined by theoretical and numerical thermo-mechanical modelling.

In the authors vision also it is necessary an integrated approach in which all the possible assessment methods are smartly merged in order to produce the largest amount of information, see Figure 1.

With the aim of presenting a general procedure for RC assessments after fire, in this work several methods are presented and tested referring to an interesting real case-study: visual examination, destructive and non destructive tests like pull out, sonic and ultrasonic test, sclerometer and SonReb test (see for example [21–24]) can produce a detailed set of data related to the mechanical characteristics of materials. Other effective techniques capable of determining fire damage on concrete are: microscopic analysis (optical and electronic), see [25–31], Thermogravimetric analysis (TGA), combined with Differential Thermal Analysis (DTA), see [32–33], X-ray diffractometry (XRD), see [34–35] and colorimetry, see [31], [36–38].

The entire data set resulting from the above mentioned techniques is the base for an integrated assessment approach. It can define the thermal events path through the identification of the related isotherms and, consequently, can quantify the extent of repairs or demolition of damaged concrete.

In this paper, after a brief description of the real fire scenario in Section 2, the integrated approach is developed and its results are discussed and presented in Section 3 with the final aim of structural assessment. In Section 4, some comments and concluding remarks are provided.

2 Scenario Description

On the evening of November 16, 2013, fire spread through a Reinforced Concrete industrial warehouse on the outskirts of the city of Cagliari (Italy). Due to the fire, which lasted approximately 8 hours and was extinguished principally with water, the central part of the building and its load-bearing structure were damaged.

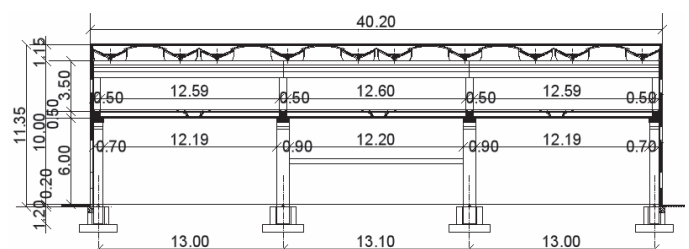
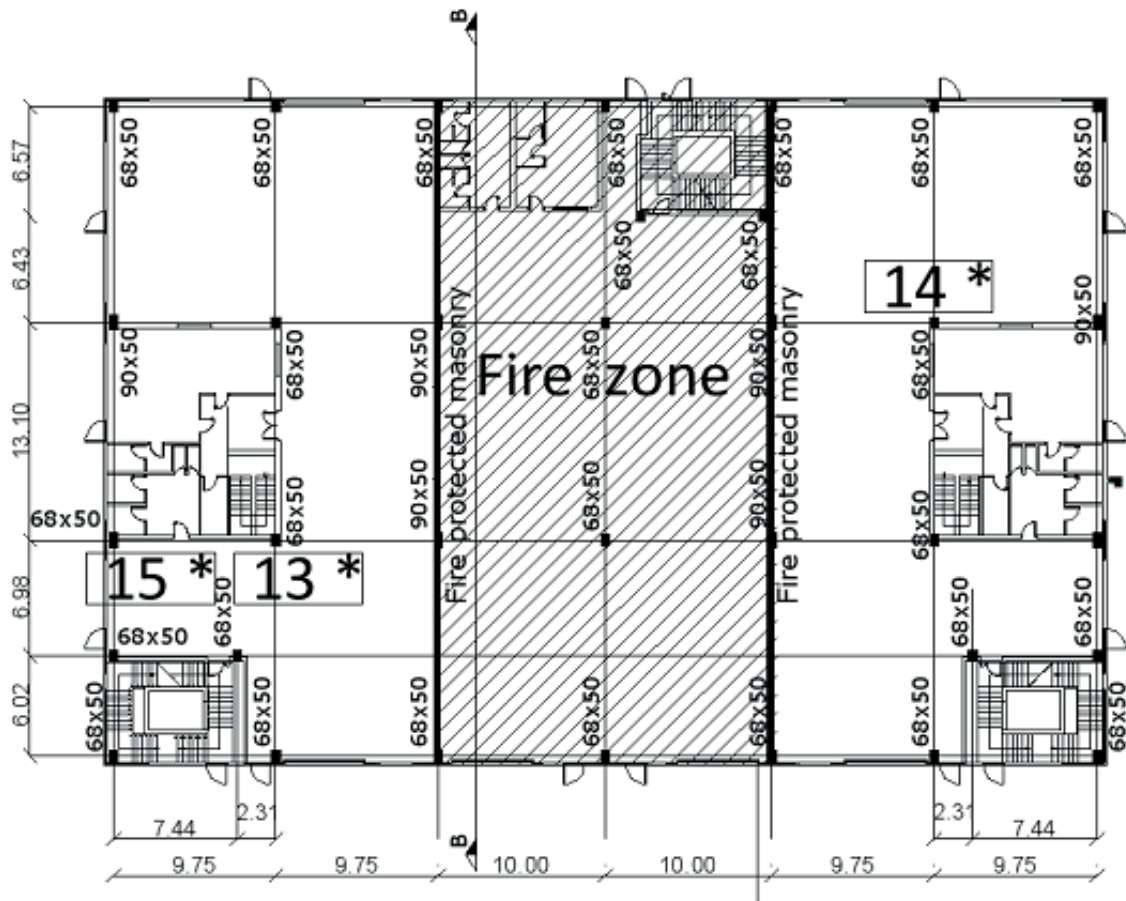
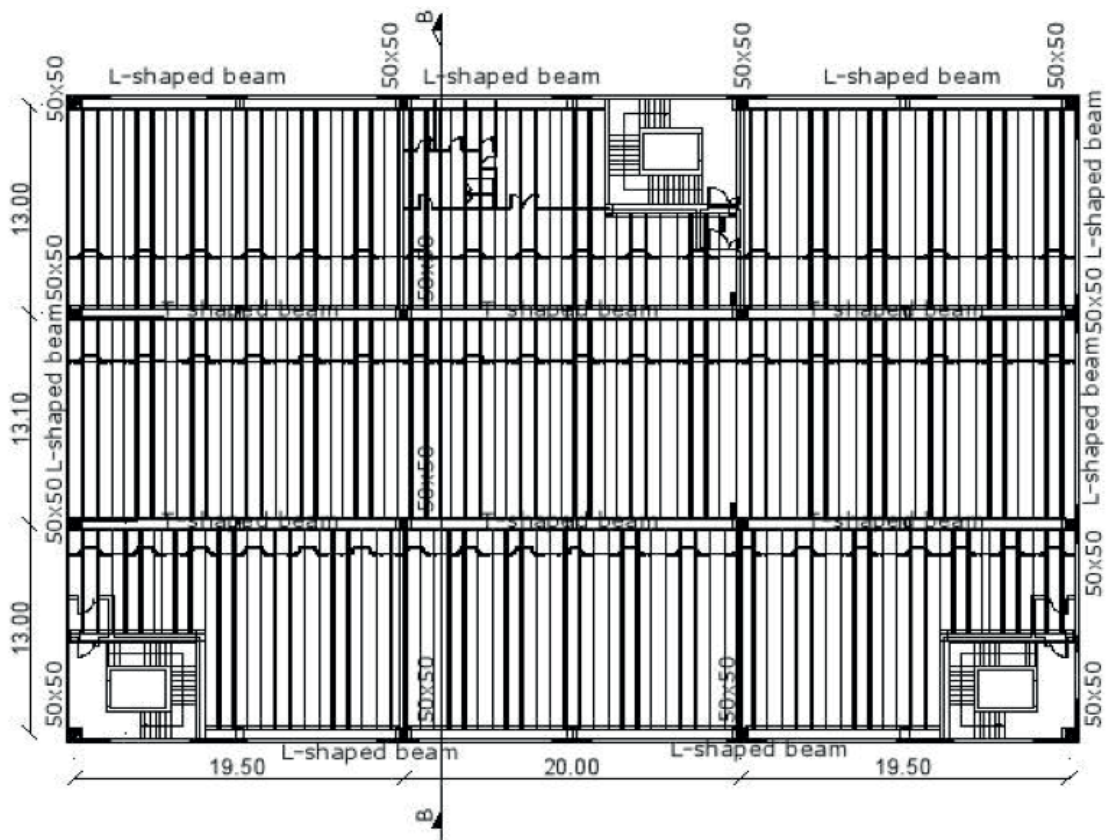


Fig. 2 Cross-section B-B of the structure. All dimensions are in m.

The industrial warehouse was designed in 2008 and built in 2010. It consists of a ground and first floor; plant dimensions are approximately 60×40 m, the first floor height is 6.0 m, while the maximum height is 11.1 m.



(a)



(b)

Fig. 3 Plant view of the ground floor (a) and of the first floor (b) with the fire zone highlighted. Plant dimensions are expressed in m, while cross-section measurements are expressed in cm. The top figure (a) presents the position of columns 13*, 14* and 15*, outside the fire zone, used as a reference (non-damaged) elements.

The load-bearing structure is a precast reinforced concrete frame (see Figures 2 and 3), with a R.C. slab cast on site representing the extrados of the first floor).

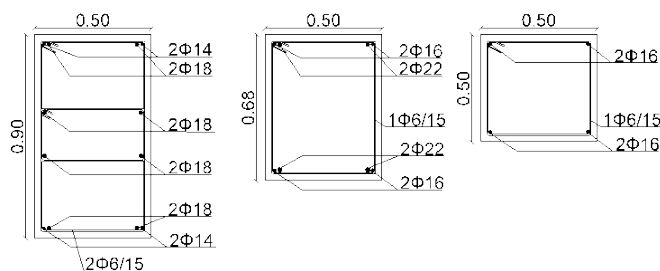


Fig. 4 Typical cross-sections of columns with the reinforcement arrangement. Cross-section measures are in m, while reinforcement diameters are in mm.

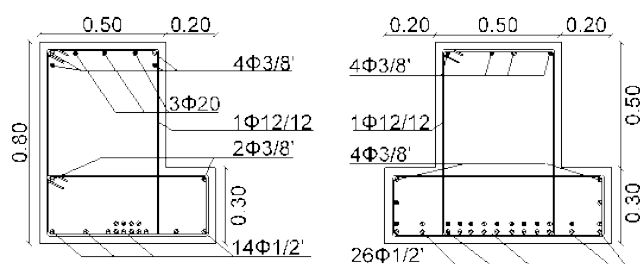


Fig. 5 Cross-section of an L- and T-shaped beam with the reinforcement arrangement. Cross-section measures are in m, ordinary reinforcement diameters are in mm, while pre-stressing tendon diameters are in inches.

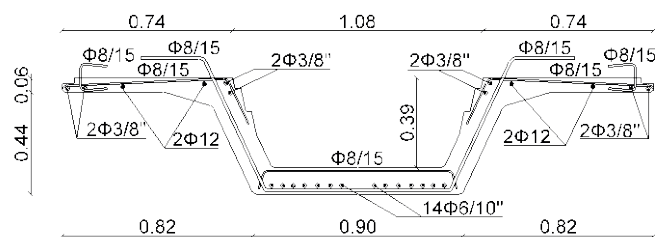


Fig. 6 Cross-section of omega-shaped transversal beams with the reinforcement arrangement. Cross-section measures are in m, ordinary reinforcement diameters are in mm, while prestressing tendon diameters are in inches.

The columns on the ground floor form a net of approximately 10×13 m, where the former distance represents the span of the longitudinal beams (T- or L-shaped) and the latter the span of the transversal beams (omega-shaped). All beams are prestressed reinforced concrete elements.

The ceiling of the first floor is composed of wing-shaped girders, which are not important for the analysis presented in this paper as they were not exposed to the fire.

The basic elements of the structural frame are:

- Precast RC column with rectangular cross-section whose dimensions vary between 68×50 cm to 90×50 cm on the ground floor and are equal to 50×50 cm on the first floor. Reinforcement arrangements and other details can be seen in Figure 4. Characteristic compressive concrete strength is 46 N/mm^2 , while reinforcement bars are characterized by a yielding strength of 430 N/mm^2 and a tensile strength of 540

N/mm^2 in the case of a diameter smaller than 12 mm; otherwise yielding strength is 430 N/mm^2 and tensile strength 480 N/mm^2 .

- Prestressed RC longitudinal beams of a 10 m span, with T-shaped cross-section whose dimensions and reinforcement arrangement are presented in Figure 5. The corresponding beam on the lateral side of the building is of the L-shaped type, and its characteristics and cross-section are also depicted in Figure 5. Concrete and ordinary reinforcement characteristics are the same as those presented for the column. Prestressing tendons are characterized by a diameter of $3/8''$ (9.5 mm) and $1/2''$ (12.7 mm); their tensile strength is 1860 N/mm^2 .
- Prestressed RC transversal beams with a 13 m span, which are omega-shaped. Their cross-section characteristics and reinforcement arrangement are shown in Figure 6, and they, along with the 90×6 cm precast plates connecting each beam to neighbouring parallel ones, represent the intrados on the first floor. Concrete and reinforcement characteristics are the same as those presented for the T-shaped beams
- Highly-reinforced concrete slab cast on the transversal and longitudinal beams of the first floor; its height varies between 10 to 30 cm and it covers the whole building area. Characteristic compressive concrete strength is 25 N/mm^2 . Reinforcements bars of 10 mm diameter are distributed in order to form a 20×20 cm net.
- Piles and connective foundation beams. Concrete and reinforcement characteristics are the same as those presented for the columns.

The cladding is composed of precast panels, directly constrained on the foundation or transversal beams. Internal partition walls, separating the ground floor into three different areas see Figure 3a, are designed to be fire-resistant. Actually, they consist of bricks covered with plaster and are characterized by a thermal insulation which guarantees a fire protection class equal to REI 120 (according to UNI EN 13501-1 [39]). This characteristic is very important, as it assures that the fire was confined only to the central part of the ground floor and did not spread to the whole building. For this reason, only the columns in the central part of the ground floor and the longitudinal and transversal beams on the first floor were affected by the fire. The ground and the first floor were covered by raw rubber mats, typical of industrial buildings. The materials stored in the warehouse were of various kinds: plastic bags, medical devices, clothes, wood, etc.

3 Assessment of the Fire Damage on Reinforced Concrete

In order to assess the damage to the structural elements the above mentioned integrated approach is developed by means of the following steps :

- Thorough analysis of the original design documentation and visual examination.
- Load test on a heavily-damaged frame in order to assess residual load-bearing capacity.
- Geometric recording of the reinforced concrete elements by means of laser scanner.
- Assessment of the quality of the structural concrete by means of destructive and non-destructive tests.
- Assessment of the quality of reinforcements by means of destructive tensile strength test.
- Assessment of the degree of damage to the concrete by means of mineralogical, microstructural and colorimetry investigations.

3.1 Visual Examination

Visual examination is the simplest and cheapest technique. A trained eye can record very interesting data regarding both the residual structural safety and mechanical characteristics after a fire. In this work, initial visual examination provided a rapid survey of the damage: the central area of the ground floor was damaged by the fire, as shown in Figure 7.

The debris (pieces of concrete spalled out from the beams and columns, plastic material, residues of steel shelving, pieces of wood pallets, etc.) produced by the fire covered almost the whole floor.

In Figure 8, a plant view of the fire zone, with labels for each structural element, is reported.

Lateral columns labelled 4–6–7–9 present the most evident damage: it seems that they have been hollowed out from the fire-exposed side towards the core, probably due to convective motion generated during the fire. Concrete belonging to these columns was expelled, leaving a visible void, while reinforcements are still present although damaged. The contrast with the neighbouring fire-resistant wall is patent as well, and is depicted in both Figure 7 and Figure 9, where it is easy to note that column 6 is severely hollowed-out. On the contrary, perimeter columns 1–2–3–10–11–12 were less exposed to the fire, and negligible visible damage was recorded.

Central columns 8–5 present a completely different situation: the superficially-burned plaster exhibits great characteristic roughness, and its colour tends towards greyish white. Spalling of concrete occurs infrequently in these elements.

The bottom part of the T-shaped beams (labelled with T in Figure 8) was exposed to the fire; indeed, the upper part was protected by the slab and by the omega-shaped beams. In particular, beams T3–T4–T5–T6 seem to have suffered the most important damage, with concrete spalling and desolidarisation of prestressing tendons.



(a)



(b)

Fig. 7 Overview of the fire-damaged area.

In Figure 9b, the situation of beam T6 and corresponding longitudinal beams is reported. The latter are visibly damaged as well: in most of these omega-shaped beams, concrete spalling is present in broad areas. Thus, in this case as well, there are areas in which prestressing tendons have lost their principal effect, becoming ordinary reinforcements. The other heavily-damaged longitudinal beams are labelled L4–L5–L8–L9 in Figure 8. As reported in the previous paragraph, the fire-resistant lateral partition wall guarantees a fire protection class equal to REI 120.

Actually, it separates the fire area from other areas, providing sufficient thermal insulation. The left wall (referring to Figure 8) was heavily damaged, with many cracks and incumbent collapse, as shown in Figure 9a. The right wall, shown in Figure 7 and Figure 9b, has lost part of its plaster, but there are no visible cracks.

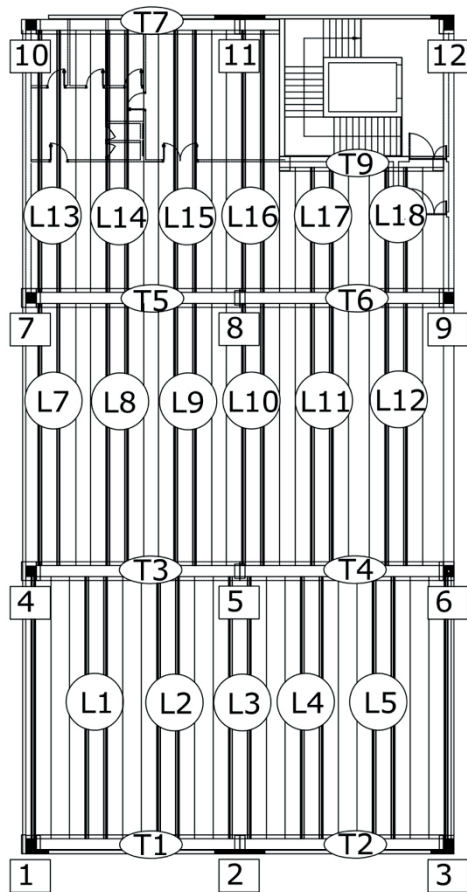


Fig. 8 Plant view of the fire area on the ground floor.

The precast reinforced concrete plates, which connect each longitudinal beam with parallel neighbouring ones, represent, along with the latter beams, the intrados of the slab separating the ground from the first floor. It was severely damaged because it was directly exposed to the fire: concrete spalling and collapse of its reinforcements, shown in Figures 7 and 9, represent the most important damage. On the other hand, the slab cast on these elements appears in good condition; there have been some thermic deflections, but structural reliability is not jeopardised, as will be shown in the following paragraphs (3.2 and 3.3).

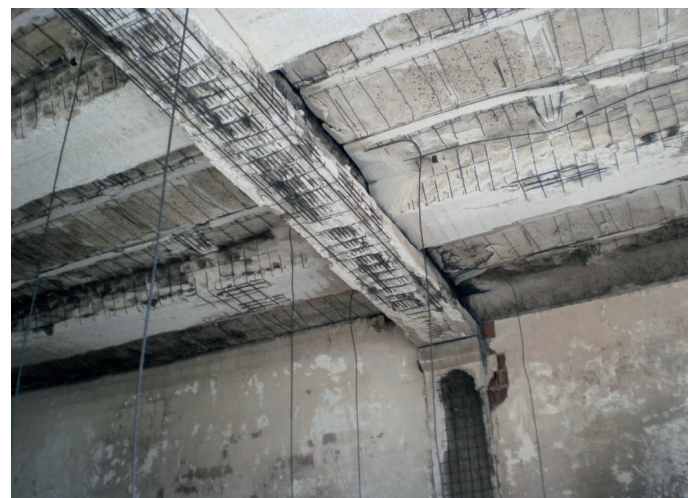
3.2 Load Testing

In order to assess the reliability and remaining bearing capacity of the structure, a direct load test was developed. The element tested was a longitudinal omega-shaped beam (corresponding to label L12, see Figure 8) having a net span of 12.2 m. The load was progressively applied to the corresponding part of the slab by means of a water dam, characterized by a width of 3 m and a length of 6 m. Considering that beam span is greater than the latter length, an equivalent water load was estimated (6.1 kN/m^2) and provided to the dam in order to produce the same bending moment obtained by a service load of 4.0 kN/m^2 .

Three displacement transducers, characterized by an accuracy of 0.01 mm (Ch3–Ch4–Ch5), were positioned at the intrados of beam L12 according to the scheme reported in Figure 10a. In this way, it was possible to record deflection at mid-span (Ch4), at the end of the beam (Ch3) and mid-span deflection of the neighbouring beam labelled L11 (Ch5). The load was applied in subsequent steps, varying the amount of water contained in the dam. Displacements at the above-mentioned three points were continuously recorded and are represented in Figure 10b.



(a)



(b)

Fig. 9 Lateral cladding cracks (a), T-shaped beams, girders and lateral column damage (b).

It is important to mention that the structure had never been tested under service load; for this reason, inelastic settlements were expected. In addition, the slab slope forbade uniform water distribution in the dam during the initial test phase, when the dam was not full. These facts explain why, after unloading, a midspan deflection of 0.62 mm is still present.

Despite these data, global elastic behaviour was still present after the fire, and finally, maximum deflection (2.80 mm) was recorded at mid-span under a water dam load of 6.1 kN/m^2 .

The RC slab supported by the beam tested plays a structural role which is not negligible; this is proven by the deflection recorded by Ch5. Stress distribution due to this effect also reduced beam deformation during the fire.

side and allowing estimation of the centre-of-gravity position. Both ends of each column were considered constrained and not exposed to fire, and variations in their centre-of-gravity position considered negligible.

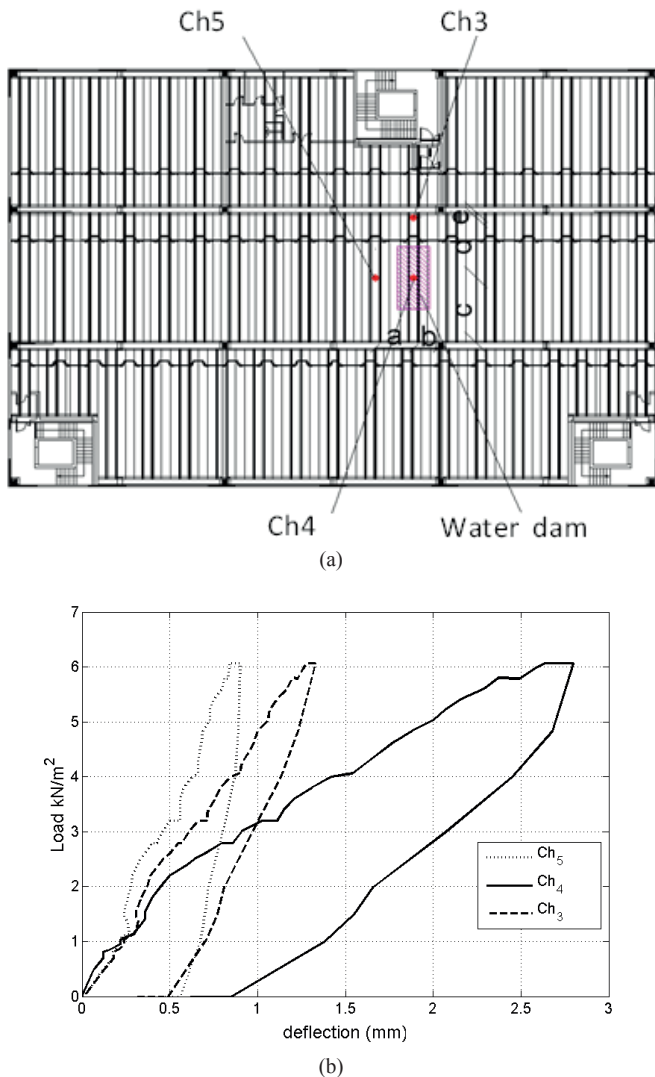


Fig. 10 (a) Positions of displacement transducers and the water dam during the loading test, a = 3.55 m, b = 2.27 m, c = 6.30 m, d = 5.80, e = 0.50 m. (b) Load-displacement diagrams for the three transducer recordings.

3.3 Geometrical Survey by means of Laser Scanner

A thorough geometrical survey was developed by means of a Faro-Focus 3D Laser Scanner, characterized by an absolute error below 2 mm for a scanning distance between 10 and 25 m. Its horizontal and vertical resolution is equal to 0.009°. It is also characterized by an image acquisition speed of 976000 pt/sec by means of an integrated digital camera with 70 megapixel resolution. Column geometry after the fire (with a total height of 6 m and a rectangular cross-section) was recorded by laser scanner; obviously, these elements were also damaged. For this reason, at least four sections at different heights (Section 1, 1 m; Section 2, 3.2 m; Section 3, 3.6 m; Section 4, 5.2 m) for the six central columns (labelled 4 to 9, see Figure 8) were scanned (see Figures 11–13), detecting the fire-exposed

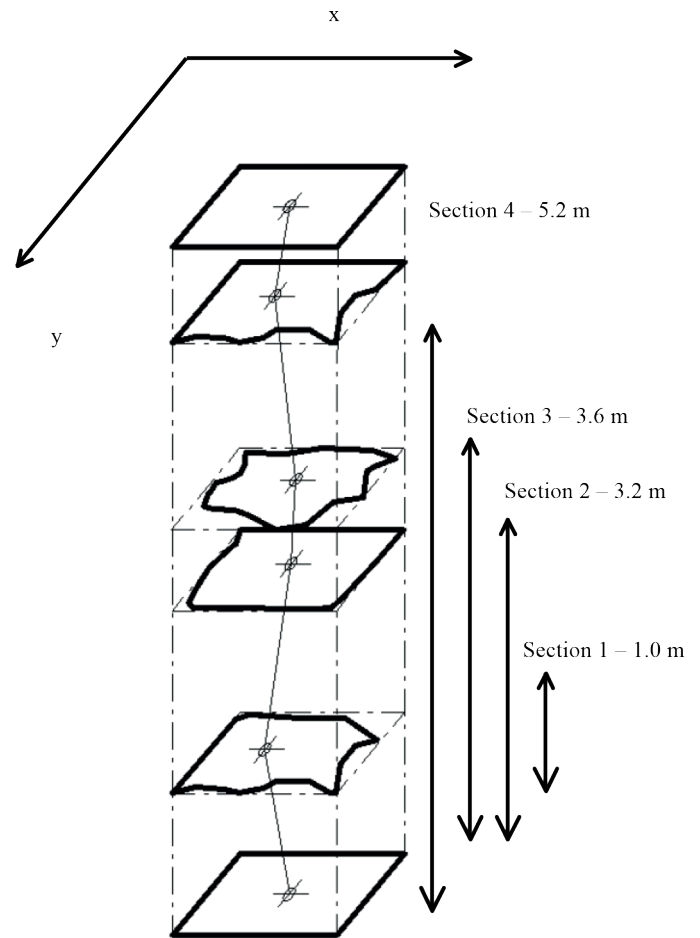


Fig. 11 Scheme of column cross-section center-of-gravity detection.

Concerning the central columns (8 and 5), it was possible to record the whole perimeter, while in the case of lateral columns (4,6,7,9), only one side was exposed to the fire and consequently recorded. In the latter case, the centre-of-gravity position was determined considering design characteristics for the other 3 sides. In this way, it was possible to study the variation of this position through column height, see Figure 12. In this Figure, the effect of the fire-induced deformation is clearly visible and tends to concentrate centre-of-gravity position variations in the central part of the column (Sections 2 and 3, see Figure 11), confirming the assumptions of constrained ends for each column. Column 6, characterized by a 90 × 50 cm cross-section, was dramatically hollowed-out during the fire and presents the most important variations, equal to 40 mm in x direction and 12 mm in y direction. It is important to mention that the position of the centre of gravity is influenced by section damage, and in particular for Column 6, these displacements do not necessarily involve deformation of the non-exposed sides. Columns 8 and 5, characterized by a 68 × 50 cm cross section, were exposed along their whole perimeter but present

very few centre-of-gravity position variations: less than 10 mm in the former case and less than 5 mm in the latter.

In Table 1, the Standard Deviation (SD) defined in the following Eqn (1) was evaluated, considering the position of the centre of gravity:

$$SD_x = \sqrt{\frac{\sum_i (x_i - \bar{x})^2}{n-1}}; SD_y = \sqrt{\frac{\sum_i (y_i - \bar{y})^2}{n-1}} \quad (1)$$

where x_i, y_i are the centre-of-gravity coordinates for the i -th cross section and \bar{x}, \bar{y} are the average coordinates considering all the n sections of a chosen column.

Table 1 Standard deviation of the center-of-gravity position for some columns on the ground floor, considering four cross-sections at different heights.

Column	SD x (m)	SD y (m)
4	0.0168	0.0037
5	0.0037	0.0021
6	0.0170	0.0064
7	0.0095	0.0020
8	0.0030	0.0034
9	0.0086	0.0037

Only columns 4 and 6 show a SD x higher than 10 mm, while in all other cases, it is unlikely to find values greater than 5 mm. These centre-of-gravity position variations represent a small fraction of column height, in addition, as stated previously, they are probably due to local damage of the cross-section and not to real displacement of the column, see Figure 13. Furthermore, after a complete section restoration with new concrete, variations will be reduced to completely negligible values.

The fire also damaged the whole central area of the ground floor, and transversal T-shaped beams (labelled with T code in Figure 8), simply supported by the columns, were deformed and modified. Transversal omega-shaped beams (labelled with L code in Figure 8), supported by the above-mentioned T-shaped beams, consequently experience constraint displacement δ , which determines rigid rotation α , as schematised in Figure 14.

For this reason, absolute deflection v recorded by the laser scanner for each beam must be purged from the deflection, due to rigid rotation α , in order to determine actual deflection rv . The entire span length L , absolute and actual deflection v and rv , respectively, and also the location of maximum deflection y and rigid rotation α for each beam are reported in Table 2. The negative sign indicates upward deflection, while the positive one refers to downward deflection.

Considering the T-shaped beams (corresponding to code T, see Figure 8), higher negative deflections are located on the right side of the plant (beams T2–T4–T6), while the other beams (T1–T3–T5–T7–T9) present positive ones (see Figure 8). It must be considered that each beam is designed with a

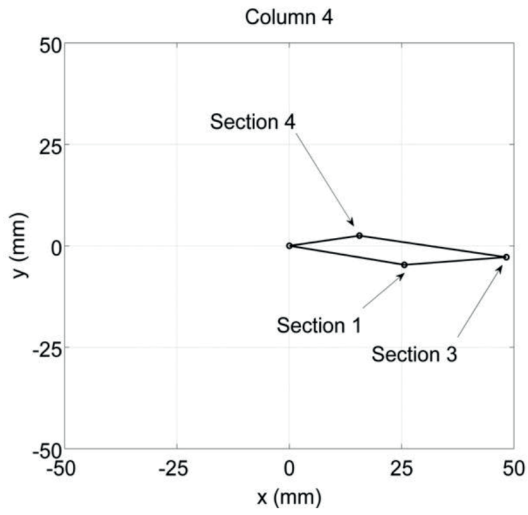
negative deflection due to the prestressing tendons useful in reducing deflection of the beam under service loads. Local damage and global deformation yield the above-mentioned values.

A different situation can be deduced from analysis of the longitudinal omega-shaped beams (corresponding to label L, see Figure 8). In the lower part of the plant, deflection values corresponding to beams labelled L1 and L4 are quite important, with a peak of 74.23 mm, corresponding to 6/1000 of the span of the L4 element. This value proves that the effect of the fire, in addition to the dead load of the structure, removed initial negative deflection (equal to 25–30 mm, see the undamaged beams labelled La and Lb located outside the fire zone) present in all L-beams, in only a few damaged elements. In most other cases, the deflection value is still negative, proving that prestressing action is still active in several beams and girders.

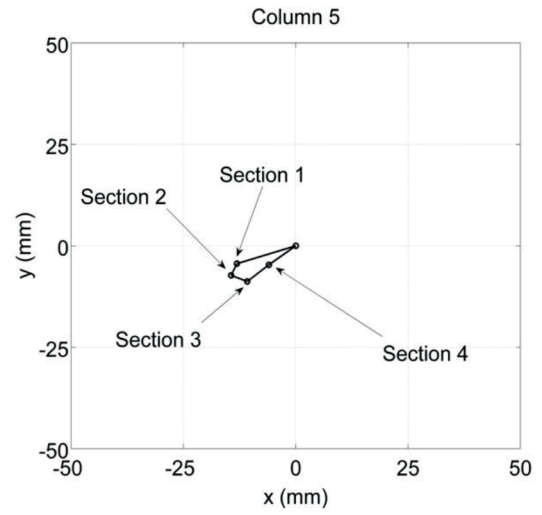
Local damage of beams has not been considered in the deflection estimation. The real damaged and deformed profile was represented by a spline curve in order to reconstruct the theoretical deformed curve without local damage. In this way, greater accuracy was obtained.

First-floor slab deflection was also investigated by means of a Laser Scanner, and results are reported in Figure 15. The maximum deflection of 60 mm is indicated by the black lines located on the left side and in the bottom part of the fire area. Both of them correspond to a midspan beam point.

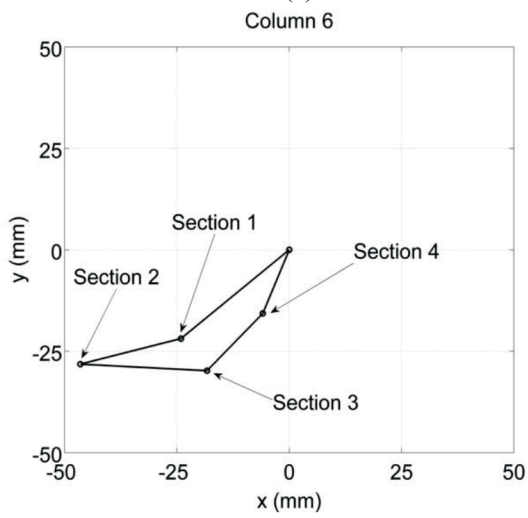
Despite the high value of maximum deflection (60 mm), there are no visible cracks in the extrados, and the only other sign of the fire is the floor discolouration.



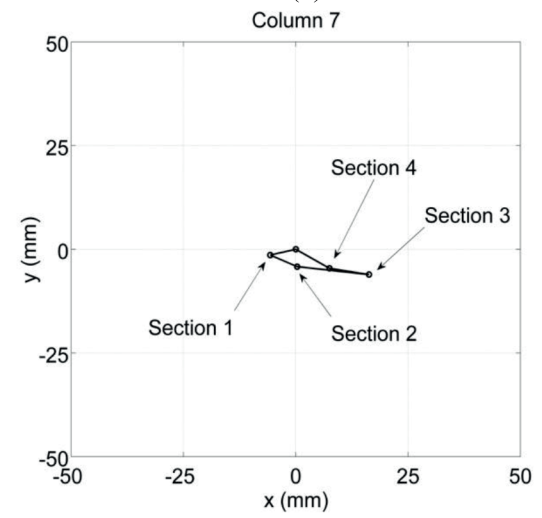
(a)



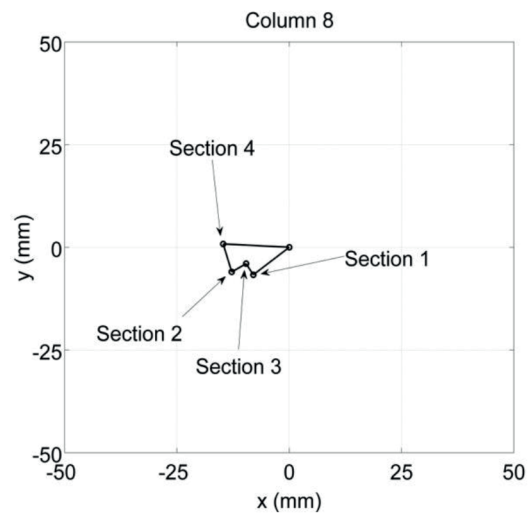
(b)



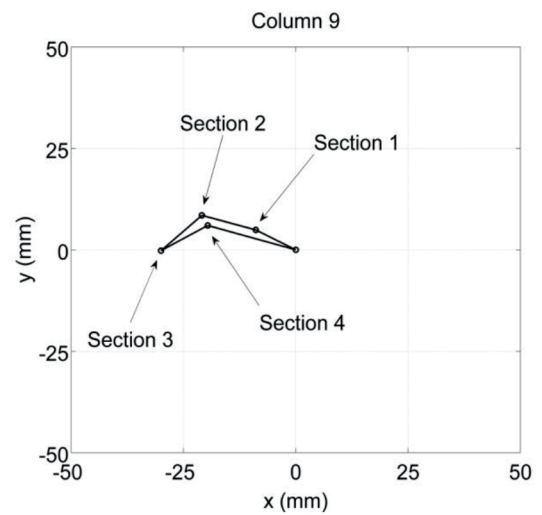
(c)



(d)



(e)



(f)

Fig. 12 Centre-of-gravity position of column cross-sections at different heights.

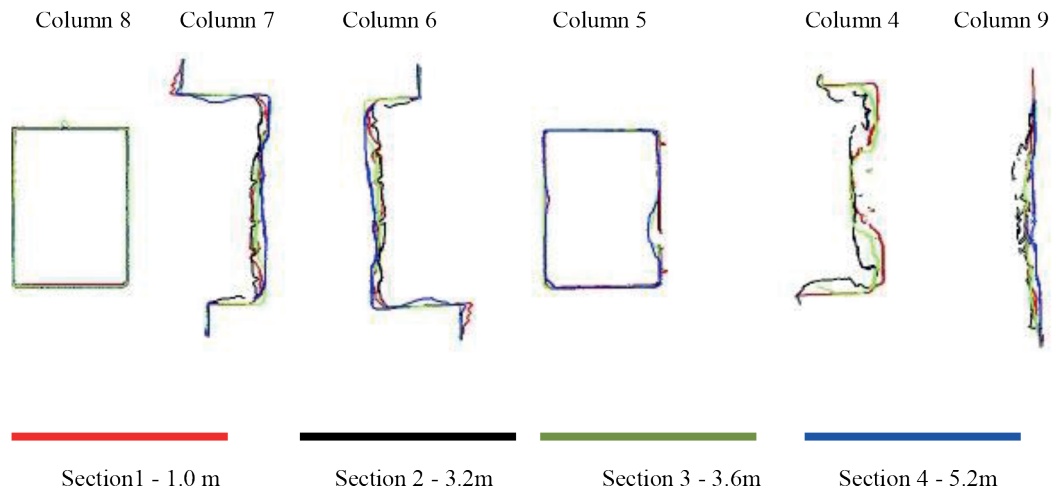


Fig. 13 Fire-exposed side of column cross-sections at different heights, recorded by means of a laser scanner.

Table 2 Beam deflection recorded by means of a laser scanner.

Beam	L (m)	v (mm)	y (m)	δ (mm)	r_v (mm)	α (deg)
L1	12.28	80.70	6.52	14.80	72.84	0.07
L2	12.29	22.10	12.14	24.70	-2.30	0.12
L3	12.25	36.20	12.15	38.20	-1.69	0.18
L4	12.23	91.20	8.17	25.40	74.23	0.12
L5	12.26	39.90	7.65	23.60	25.17	0.11
L7	12.21	-23.40	6.97	1.60	-24.31	0.01
L8	12.26	-12.30	9.10	-7.00	-7.10	-0.03
L9	12.25	-14.90	10.32	-10.50	-6.05	-0.05
L10	12.22	-30.90	10.20	-22.00	-12.54	-0.10
L11	12.30	-19.20	3.67	-15.10	-14.69	-0.07
L12	12.24	-23.50	5.80	-7.20	-20.09	-0.03
L13	11.85	-25.20	6.65	-2.60	-23.74	-0.01
L14	11.92	-19.10	6.34	-1.00	-18.57	0.00
L15	11.89	-12.20	5.47	1.60	-12.94	0.01
L16	12.25	-31.00	8.57	-10.60	-23.58	-0.05
L17	5.57	-11.90	0.97	4.80	-12.74	0.05
L18	5.67	-9.10	4.17	-27.00	10.76	-0.27
La	12.23	-36.70	7.97	-13.80	-27.71	-0.06
Lb	12.25	-32.10	9.30	-15.90	-20.03	-0.07
T1	9.20	63.10	8.79	60.10	5.68	0.37
T2	9.33	-28.60	6.22	-0.20	-28.47	0.00
T3	9.35	32.60	8.83	32.60	1.81	0.20
T4	9.35	-11.90	3.65	-17.70	-4.99	-0.11
T5	9.35	31.00	3.75	32.10	18.13	0.20
T6	9.35	-26.00	4.83	-30.30	-10.35	-0.19
T7	9.33	12.00	1.41	15.70	9.63	0.10
T9	6.84	29.80	6.76	30.00	0.15	0.25

It is interesting to point out that Figure 15 can also represent a synthetic map of structural fire damage; indeed, it highlights the most deformed area, corresponding to beams T5, L4 and L5.

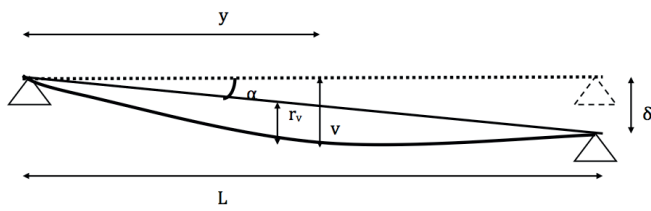


Fig. 14 Scheme of beam constraint displacement.

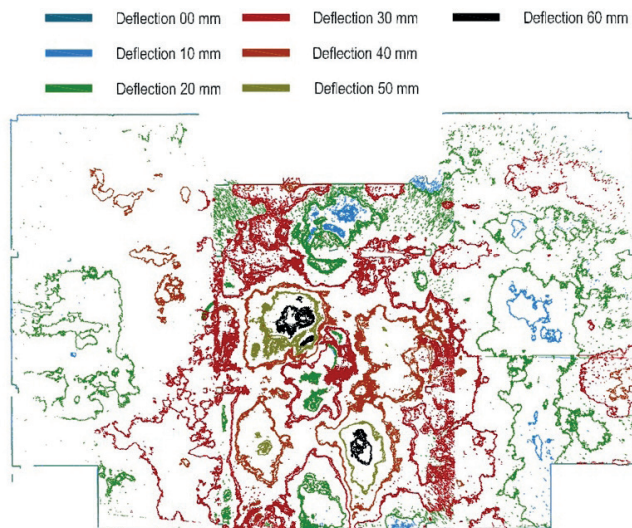


Fig. 15 First-floor slab deflection.

3.4 Non-Destructive Tests

Sonic and ultrasonic tests on RC structures can be very useful due to the well-known correlation between the sonic pulse through concrete and its density. These techniques can produce a detailed set of data related to the mechanical characteristics of materials, see for example [21–24] and [40–41]. In particular, the velocity of ultrasonic transit pulses in undamaged concrete can reach and exceed 5000 m/s, see [22]. Its value may decrease significantly in the presence of defects caused by exposure to fire.

In addition, the concrete mixture has such a great influence on the correlation that it cannot be considered unique. Nevertheless, speed variations in waves recorded in the same element can effectively discriminate between damaged and undamaged areas.

On the first-floor slab, sonic tomography was carried out by means of an indirect (surface transmission) sonic pulse velocity test on the green area highlighted in Figure 16. A grid of 1x1 m was defined and 8 significant points (labelled from A to H in Figure 16) determined.

Then the Boviari RSG-55 piezoelectric receiver was placed on each significant point and a 1.5 Kg impulse force hammer, instrumented with a piezoelectric sensor (in order to record impulse force), was applied to the neighbouring 8 points

(labelled 1 to 8 in Figure 16). In this way, the speed of 8 waves for each significant point was recorded; their average is reported in Figure 17 with the corresponding standard deviation (SD).

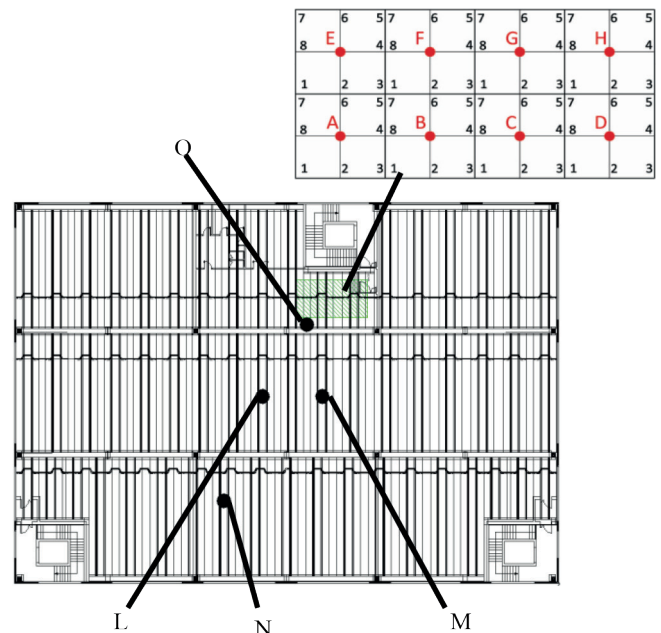


Fig. 16 First floor slab Sonic Tomography and ultrasound test positions.

From the data reported in Figure 17, it is clear that the most highly damaged area corresponds to left points A and E, which present the lowest speed (2000–2400 m/s). Indeed, it is well known (see [21]) that damage significantly reduces the speed of sonic pulses. On the other hand, points H and D present the highest speed value (3800 m/s) and are located in a corner of the slab, near the stairwell. The latter points were probably less exposed to the fire and consequently reached lower temperatures than the ones (points A and E) located in the centre of the slab.

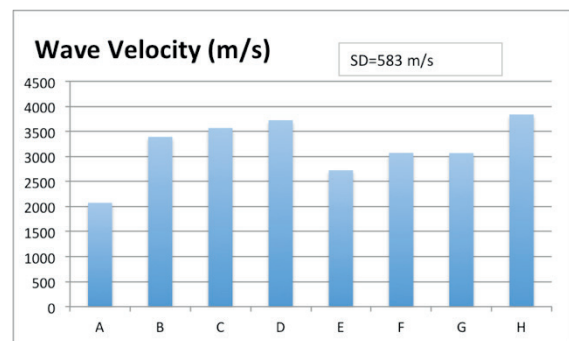


Fig. 17 First-floor slab Sonic Test chart results.

Furthermore, four cylindrical core samples of 6 cm diameter were taken from the slab at points represented by the circular black spots in Figure 16 by means of an HILTI corer DD 130. An ultrasound direct test was performed on these cores, obtaining the results presented in Table 3. These results confirm degradation of the central part of the slab corresponding to the area around beam T4.

Table 3 Ultrasound wave speed from direct test on cores extracted from the slab.

Slab Position	Core length	Speed (m/s)
Point O	85.8	1848
Point N	88.6	1818
Point L	56.6	1503
Point M	54.5	1534

The ultrasound test was performed by means of a BOVIAR TSG55 piezoelectric transmitter capable of a signal characterized by a 55 kHz frequency and 0.05 J of energy.

Table 4 Ultrasound wave speed from direct test on different columns.

Element	Core length	Position (mm)	Speed (m/s)
Column 4	115.2	1380	5319
Column 7	114.9	1550	5469
Column 9	113.8	980	5252

In order to assess the mechanical characteristics of concrete in the columns exposed to fire, several cores (also in this case their diameter is 6 cm) of various lengths were taken from different pillars. A synthesis of these results is presented in Table 4, where “Position” indicates the location of the core along the longitudinal axis of the element starting from elevation 0 mm, corresponding to the ground level, to 6000 mm, corresponding to the intrados of the first floor. The average speed value for a fire-exposed column is equal to 5430 m/s and no large variations are detected among the three columns. This result suggests that concrete mechanical characteristics are very similar for these elements and that fire damage is quite uniformly spread among them.

Comparison with the ultrasound pulse speed of cores coming from the slab, where pulse speed has an average value of 1500–1800 m/s, underlines the different mechanical characteristics of the cast concrete on-site slab and the pre-cast one in the columns.

On the same cores, a colorimetric test with a sprayed aqueous solution of 1% phenolphthalein in ethyl alcohol was performed to determine carbonation depth. It was negligible in all elements analysed (floors, columns and beams), both in those exposed to fire and those that were not, so there was no carbonation on all samples.

One of the most interesting and effective non-destructive tests is called SonReb (SONic + REBound) and consists of the combined use of the sclerometer test and the ultrasonic one (see [42] and [37]). Indeed, this technique is capable of quite accurate assessment of concrete strength in a very short time. As correctly stated by Breyse in [37], calibration is mandatory for this method; indeed, several relationships have been proposed in the literature, confirming that not only one effective formula exists for every case. In this paper, the authors present a calibration method based on a prior model defined by the following Eqn:

$$f_{cest} = a \cdot V^b \cdot R^c, \quad (2)$$

where, V is the ultrasound velocity, R is the rebound index and, according to [37], $a = 1.5 \times 10^{-10}$, $b = 2.60$, $c = 1.30$.

The average experimental strength of the concrete $f_{cest,mean}$ must be evaluated by testing at least one core extracted from the element investigated. Obviously, the larger the number of tests is, the greater the precision. Then, using Eqn (2), the average compressive strength $f_{cest,mean}$ of the elements is calculated. A calibration parameter k equal to $f_{cest,mean}/f_{cest,mean}$ is introduced into Eqn (2) in order to define the following calibrated formula for concrete strength estimation by means of SonReb:

$$f_{cest} = (a/k) \cdot V^b \cdot R^c, \quad (3)$$

This calibration method is suitable when the number of experimental destructive data provided by the core compressive test is low (below or equal to 5 specimens, see [37]).

In order to estimate the concrete strength of fire-damaged and undamaged columns, the sclerometric rebound index was measured on the “sound” part of the concrete surface of columns 4–7–8–9 (damaged) and columns 13*–14*–15* (undamaged, belonging to areas not exposed to fire).

Table 5 Sclerometric rebound index and ultrasound pulse velocity from tests on damaged and undamaged columns.

Element	Rebound Index R	Ultrasound Pulse velocity (m/s)
Column 4	56	4020
Column 7	55	3975
Column 8	56	3483
Column 9	58	4365
Column 14*	56	4857
Column 15*	60	4972

Rebound tests were performed by means of a Boviari sclerometer and were statistically analysed (a 15×15 mm grid of 22 points on each element was tested); average values are reported in Table 5. The same Table reports the ultrasound wave speed obtained by means of a direct test on the analysed elements.

Then, from columns 4–7–9 and 14* (located outside the fire zone, see Figure 3), 6 cm-diameter cores were extracted and a compressive destructive test performed. The corresponding results f_{cest} are reported in Table 6 and discussed in detail in the next paragraph. Calibration was performed on these elements; in order to take fire damage into account, two values for parameter k were determined: one for damaged columns 4–7–8–9 ($k = 1.62$) and the other for the undamaged ones: 14*–15* ($k = 2.13$), see Figure 3. Values from the estimated compressive strength test obtained from Eqn (2) and from the calibrated Eqn (3), with the experimental values obtained by means of the destructive tests, are represented in Table 6.

Table 6 SonReb method performance for the estimation of concrete strength.

Element	fc _{est} without calibration (N/mm ²)	fc _{exp} (N/mm ²)	fc _{est} with calibration (N/mm ²)	Absolute error (%)
Column 4	51	28	31	11.26
Column 7	48	40	29	25.56
Column 8	35	na	21	-
Column 9	66	33	40	20.94
Column 14 *	83	30	39	28.05
Column 15*	96	na	45	-

The calibrated estimations of concrete strength are quite similar to experimental ones; the percentage error, reported in Table 6, varies between 11% and 28%, very low in comparison to the errors produced by un-calibrated estimations.

3.5 Destructive Tests

The compressive strength test on cores sampled from damaged structural elements is one of the most reliable tool to investigate the fire influences on the concrete characteristics. A thorough post fire investigation should rely on coring if it is possible. Thus, in this case several 6 cm-diameter cores, extracted from columns and the slab, were subjected to a compressive strength test by means of a 1000 kN Comazzi machine.

Table 7 Compressive strength of cores extracted from columns and first floor slab.

Element	Strength (N/mm ²)
Column 4	28.0
Column 5	31.0
Column 7	39.7
Column 9	33.4
Column 13 *	47.3
Column 14 *	30.3
Column 14 *	17.1
Point O	15.6
Point N	17.0
Point L	24.8
Point M	18.1

Table 7 reports results concerning both the columns exposed to fire (4–5–7–9), with an average value of 30.6 N/mm² and the undamaged columns (13*–14*), whose average compressive strength is 30.5 N/mm². This result proves the homogeneity of the precast concrete. In particular, it can be pointed out that the concrete cover presented the principal visible damages, but cores were extracted from the inner part of the column, after having eliminated the damaged cover. The thermal insulation provided by the cover was probably sufficient to preserve the mechanical characteristics of the inner concrete.

Slab core (points O,N,L,M, see Figure 16) compressive strength test results confirms the difference in mechanical

concrete characteristics between the slab cast on site and precast columns. Indeed, the former presents an average value of 20.0 N/mm², lower than 30.6 N/mm² corresponding to the latter. In order to assess the mechanical properties of the reinforcement bars in the columns and in the first-floor slab after the fire, samples were also taken for strength test from Column 4, Column 9 and from the reinforcements in the intrados of the slab. The tensile strength test was performed by means of a 2000 kN Metromom machine. In the original design, reinforcement characteristics should have been 430 N/mm² yielding strength and 480 N/mm² ultimate strength for bars with a diameter under 12 mm and 540 N/mm² for bars with a diameter greater than 12 mm.

Table 8 Mechanical characteristics of reinforcement bars: Φ is the diameter in mm, f_y is the yield strength in N/mm², f_t is the tensile ultimate strength in N/mm² and e is the percentage elongation.

Sample	Φ	f_y	f_t	f_t/f_y	e
Slab Reinf.I	12	324	491	1.52	22.2
Slab Reinf.II	12	341	493	1.45	20.3
Column 4 I	18	513	534	1.04	5.3
Column 4 II	18	504	626	1.24	17.4
Column 4 A	14	338	500	1.48	21.2
Column 4 B	14	398	525	1.32	7.0
Stirr. Col. 4 I	6	287	420	1.46	18.8
Stirr. Col. 4 I	6	287	406	1.41	19.3
Column 9 I	18	491	625	1.27	11.0
Column 9 II	18	488	611	1.25	13.1
Column 9 A	14	475	597	1.26	9.5
Column 9 B	14	499	616	1.23	10.3
Stirr. Col. 9 I	6	274	400	1.46	19.2
Stirr. Col. 9 II	6	259	413	1.59	12.6

As it is shown in Table 8, in the case of Φ 18 mm diameter, all the bars analysed reach the design ultimate tensile strength value. The same good results were obtained for Φ 12 mm and Φ 14 mm bars taken from column 9, while stirrups Φ 6 mm show a decrease in ultimate tensile strength of 15%, and Φ 14 mm bars extracted from column 4 present a 5% reduction in the same characteristic. A reduction in yielding strength is recorded for all bars except Φ 18 mm – Column 9 and Φ 18, Φ 14 mm – Column 9.

These results prove that the fire did not cause a significant decrease in the mechanical properties of reinforcements; the concrete cover probably protected them with an effective thermal insulation.

3.6 Microstructural and Colorimetry analysis

In order to assess the degree of damage in fired concrete, it is very important to reconstruct the thermal path. For this reason, in addition to the above-described tests, several other analyses were developed with the aim of determining the maximum temperatures reached during the fire.

Table 9 Position of the samples analysed in the following paragraphs, as regards the columns (COL); the longitudinal axis (l.a.) starts from the ground and reaches 6000 mm at the end of the ground floor. Concerning the slab and beams, the longitudinal axis starts from the top part (or from the left part) and increases as it goes down (or right) with respect to Figure 8 and Figure 3.

Sample Label	Element	Position l.a. (mm)
COL 4 A	Ground floor Column 4	1380
COL 5 A	Ground floor Column 5	1060
COL 5 B	Ground floor Column 5	4730
COL 7	Ground floor Column 7	1550
COL 8A	Ground floor Column 8	4580
COL 8B	Ground floor Column 8	1400
COL 9A	Ground floor Column 9	980
COL 9B	Ground floor Column 9	4360
Beam 3	First floor Slab, located above beam L3	34
Beams 8-9	First floor Slab, area covering beam T6	221
Beams 8-9 (a)	First floor Slab, area covering beam T6	133
Beams 8-9 (b)	First floor Slab, area covering beam T6	230
Beams 8-9 (c)	First floor Slab, area covering beam T6	135
COL 4A SP a	Ground floor Column 4, 0.5 cm depth	1200
COL 4A SP b	Ground floor Column 4, 1.5 cm depth	1200
COL 4A SP c	Ground floor Column 4, 2.5 cm depth	1200
COL 4A SP d	Ground floor Column 4, 4.5 cm depth	1200
COL 4A SP e	Ground floor Column 4, 7.5 cm depth	1200
RS	Ground Floor Column 14*	990

Indeed, investigations under the microscope (Optical and Electronic) allow the highlighting of both the changes induced in the mineralogical phases and the degree of damage produced in the concrete microstructure exposed to fire. These changes can be related to the temperature and duration of exposure to fire.

Microcracking in the cement matrix and sometimes in the aggregates, detachment of the latter from the cement paste due to differential thermal expansion, in particular in the transition zone, and chromatic alterations are the most common effects that can be observed in fire-damaged concrete (see [25–31]).

Microscopic analysis can be developed in polarising and fluorescent light mode (PFM), (see [27], [30]). In this case, it is also capable of identifying microcrack length and width and the presence of secondary porosity in the cement matrix [25], caused by exposure to fire.

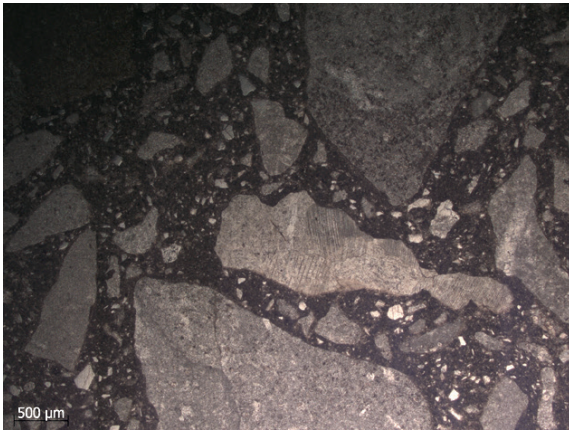
Some cylindrical core samples, (variable length and 6 cm in diameter), were extracted at different heights by dry coring from some structural elements, (see Table 9 and Figure

8). Other irregular samples expelled by the explosive spalling (SP) from columns and beams were collected. These samples were immediately sealed with a polymeric film (parafilm) and then transferred to the laboratory for diagnostic investigation. A core sample of undamaged concrete (reference sample RS, see Table 9) was also collected from column 14* (first floor, not exposed to fire, see Figure 3). The samples were de-sealed on the day the investigation started, photographed and examined using a binocular microscope.

Fig. 18 Cracks around the perimeter of aggregates and inside the reddish aggregate (sample label: Beam 3).



Fragments of the cementitious matrix were obtained using a diamond disc milling cutter. They were distinguished considering their distance from the top surface of the core, which is the one exposed to fire. Fragments were micronised in agate mortar and the powders analysed using X-Ray Diffraction (XRD) and Differential Thermo-Analysis (TG-DTA) techniques. The former analysis was performed with a Rigaku Miniflex II X-Ray diffractometer, operating at the following conditions: monochromatic CuK α radiation, 15 kV, 30 mA, sampling 1.00 2 θ /min and step size 0.0200 2 θ .



(a)



(b)

Fig. 19 Microphotographs of RS undamaged concrete: a) PPTL (Plain Polarized Transmitted Plain Polarized Light) b) CPL (Cross Polarized Light).

Mineral identification was carried out by X'Pert Philips software. Thermal analysis (TG-DTA) was performed by means of a Netzsch apparatus Jupiter 499 IV, operating with a heating rate of 10 °C/min up to a temperature of 1100 °C by flushing a protective gas (nitrogen and oxygen 80%–20%), flow rate 80 l/min. Data were processed using Proteus Netzsch software.

Some slices were also cut from the most damaged sample, following the longitudinal axis of the cylindrical core. These slices were embedded in epoxy resin and then glued on glass slides. Thin sections (30 μm thick) were obtained by a microtome Buelher Microthin apparatus. Optical observations were carried out on polished thin sections using a Carl Zeiss microscope (Axioscope 40 equipped with an Axiocam HR camera) operating in PPTL (Transmitted Plain Polarized Light) and CPL (Cross Polarized Light) mode. SEM (Scanning Electron Microscopy) studies were performed on thin sections and fragments by a Zeiss Evo LS15 apparatus equipped with a LaB6 filament as an electron source. Finally, colorimetric measurements were carried out by a Konica Minolta spectrophotometer (mod. CM 700d/600d) according to the CIE Lab Colour Space (1976).



(a)

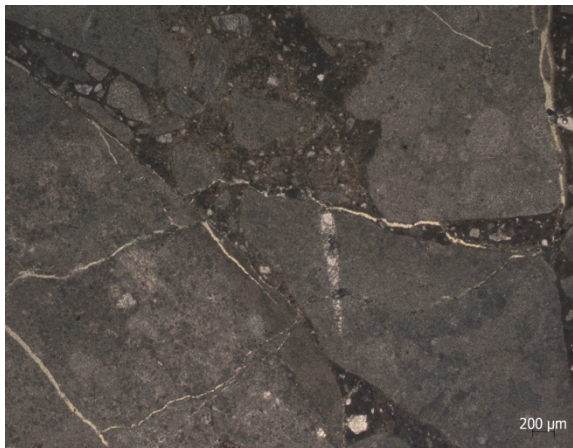


(b)

Fig. 20 Microphotos of damaged concrete surface in RL mode: (a) microcracks radiating from a macropore, cement matrix altered in colour, COL 4a Sp a; (d) pulverization and whitening (Beams 8-9 a133), see Table 9.

The RS unaltered concrete (see Table 9 and Figure 3) is characterised by limestone aggregates varying in colour from light-grey to brown and ivory. Variable morphology from angular to sub-angular, a medium degree of sphericity and a maximum diameter of about 1.5 cm were observed. Aggregates were immersed in a greyish cement matrix dotted by carbonate sands derived from artificial crushing. The concrete appears very compact and generally free of macro-defects (except for some samples with macro-voids caused by entrapped air). Bleeding of the constituents does not affect the concrete, which appears free from fractures, altered reaction rims and chromatic alteration. The RS sample preserves the final white coat, applied on a finishing layer of cement paste about 3 mm thick.

On the contrary, the fire-damaged concrete (e.g. COL 4, COL 5, COL 9, BEAMS 8-9 and BEAM 3, see Table 9), is characterized by surface pulverisation, intense whitening, selective erosion and deformation. Microfracturing is widespread: fractures cut the aggregates or develop inside the transition zone (see Figure 18).



(a)



(b)

Fig. 21 Microphotos of damaged concrete surface in PPTL mode: microcracks involving the transition zone and cutting the aggregates, sample COL 5B(a); interfacial cracks, sample COL 4A(b), see Table 9.

The concrete shows a severe decrease in its mechanical performance: the sample collapsed by applying hand pressure. Most of the core cylindrical samples (e.g. COL 4, COL 5, COL 8, COL 9, BEAM 3, and BEAMS 8-9, see Table 9) show, at different depths, a reddening of the aggregates. At depths greater than 10 cm, the effects of macroscopic decay gradually decrease. The damage induced in each sample is the consequence of the thermal tonality of the event and in particular of the maximum temperature reached, time, thermal conductivity of the concrete and diffusive processes related to gas and solids. These processes are complex, as many factors can modify the scenario.

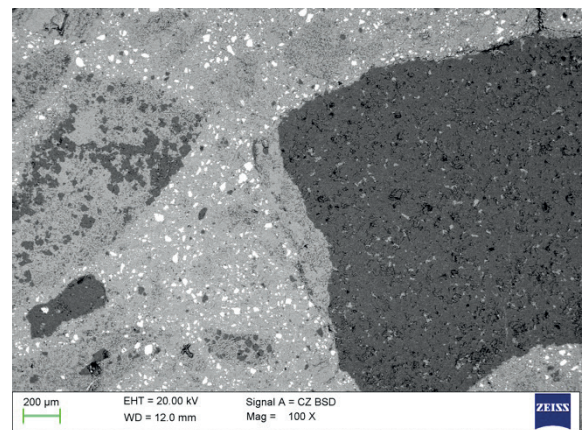
Optical microscopy (OM) is a powerful diagnostic tool [35] to reconstruct the material thermal path and, consequently, to plot isotherms. Figure 19 shows a cross-section image of the RS sample (see Table 9), observed by optical microscopy in PPTL and CPL modes. The conglomeratic aggregates exhibit angular and sub-angular shapes with a low degree of sphericity due to artificial crushing. Aggregates appear compact, without inclusions or micro-fractures.

The absence of delamination and microcracks corresponding to the transition zone was determined. In CPL mode, aggregates show a great array of interference colours typical of

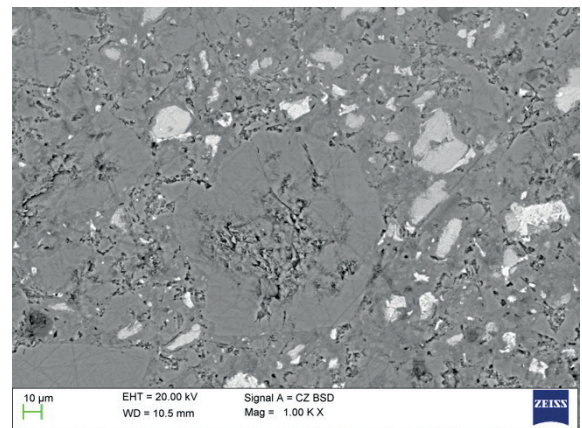
limestone. Their structure belongs to boundstone. Twinnings, calcite venules (from micritic to sparitic), and very compact bioclasts were also observed. The sand is carbonate as well. Rare clasts of quartz (of about 40 μm) were found. The cement matrix appears dark grey-brown in the CPL mode, suggesting that it is unaffected by carbonation or thermal alteration and is free of microcracks. Needle-shaped crystals of ettringite occur in large pores.

Portlandite crystals, recognizable by white spots ranging from 10 to a few tens of micrometers, occur in the cement matrix. They become more widespread in the transition zone.

The presence of rare, non-communicating pores having a pseudo-circular section, is assessed. They have been originated by entrapped air.



(a)



(b)

Fig. 22 SEM image of undamaged concrete (RS) - Overview (a); Portlandite crystal in the cement matrix (b).

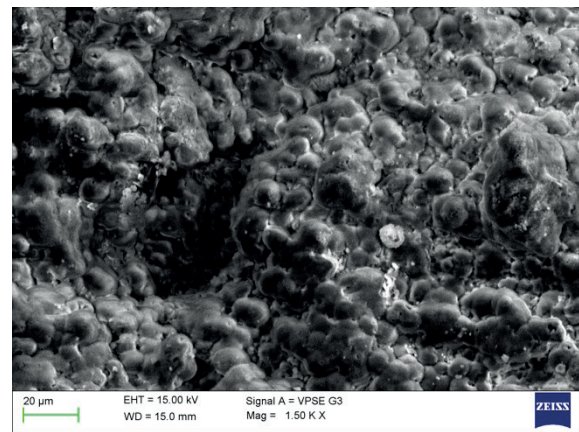
Referring to greatly-fire-damaged concrete samples (see Table 9 and Figure 20 e.g. COL 4A SP a and Beam 8-9 (b)), reflected light (RL) mode observations highlighted a zoning, starting from the surface. It is characterised by the pulverisation of aggregates and of the cement matrix, micro-scaling of clasts, differential erosion, discoloration tending to light beige of the binder and widespread microcracking (see Figure 20). Up to a depth of about 2-3 cm, significant clearing of the concrete and relevant micro-cracks were observed.

At 4–5 cm in depth from the top of some core cylindrical samples and at 10–12 cm in depth from the original surface of structural elements (columns and beams), the colour of some aggregates turned red. This redness is due to oxidation processes affecting minerals containing iron at temperatures between 300–350 °C. These reddened portions involve a thickness of at least approximately 3 cm. At greater depths, (about 10–12 cm referring to cylindrical core samples), microcracks decrease, the cement matrix appears dark grey and detachments become very rare, particularly in the transition zone. Considering the most damaged samples (e.g. COL 4, 5, 8, 9, Beam 8-9 and Beam 3, see Table 9), OM observations highlighted quite widespread microcracking. In Figure 21, the system of cracks appears bright yellow in PPTL mode. Microcracks affecting aggregates, sometimes fractured into several parts, are depicted in Figure 21a. Interfacial cracks occur in the transition zone, Figure 21b. Other microfractures tend to dissolve inside the cement matrix; their width ranges from 20 to 40 µm. In CPL mode, the cement matrix appears discoloured, and many mineralogical phases appear poorly distinguishable.

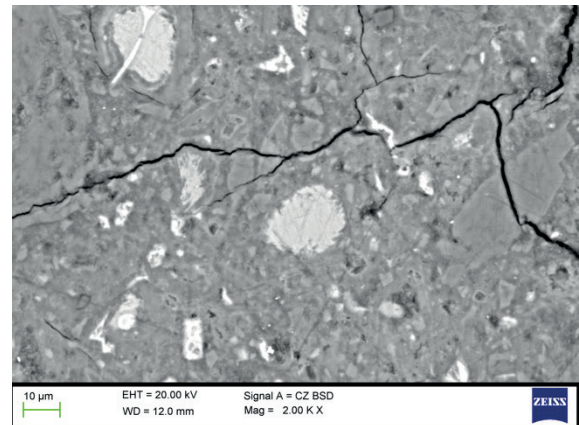
The Scanning Electron Microscopy (SEM) study of undamaged concrete (see Figure 22) shows aggregates of calcite and dolomite immersed in the cement matrix, which is not affected by microcracking (see Figure 22a). Cores of anhydrous calcium silicates and calcium aluminates exhibit great brilliance, whereas portlandite is light grey (see Figure 22b). Ettringite crystals in their typical needle-shape are also observed.

SEM investigations have produced evidence of the various damage caused by exposure to fire. Figure 23a shows globular formations on the surface of concrete of sample COL 4A. An overview of the concrete from sample COL 5B, at about 2 cm in depth, shows a widespread condition of microfracturing, see Figure 23b.

X-Ray Diffractometry (XRD) and Thermogravimetric and Differential Thermal Analysis can be very effective in determining the temperature path in fire-exposed concrete elements. Actually they can assess the changes in the physical and chemical properties of material corresponding to temperature variation. In this way, it is possible to reconstruct the temperature path and time history using some benchmark changes. For example, the depletion of primary ettringite at about 80°C and the thermal breakdown of Calcium Silicate Hydrate (CSH) and Calcium Aluminate Hydrate (CAH) gels at approximately 180–300 °C ([27], [32]) start to produce changes in mineral composition and pore size distribution, respectively, in the range of pore gel and sub-capillary pores, [33]. Actually, the most severe and irreversible damage begins at higher temperatures, particularly those at which the de-hydroxylation of Portlandite starts: [25], [30], [32].



(a)



(b)

Fig. 23 SEM image of the top of high-damage sample: (a) micrometric globular formations, COL 4A; (b) microfracturing affecting cement matrix, transition zone and aggregates, COL 5B, see Table 9.

In particular, XRD plays an important role in the characterization of concrete. It allows a definition of the nature of the crystalline species, detecting what the dominant aggregate in the concrete is, see [34], [35]. This technique can be combined with punctual Energy Dispersive X-ray Spectroscopy (EDS) microanalysis to highlight changes in the chemical composition of concrete constituents.

The most important peculiar benchmarks linked to a particular temperature, are reported in Tab.10. For example, the effect induced on the cement paste at around 500°C by the dehydroxylation of Portlandite and its conversion into Calcium oxide is well known. The latter mineral tends to rapidly hydrate itself, with a remarkable increase in volume, to produce newly-formed Portlandite. A significant increase in microfracturing and porosity is related to this transformation, induced by expansion and tension (see [32]). Even at 570 °C, the phase transition of quartz from alpha to beta, also accompanied by volumetric expansion of 5.7%, leads to increased porosity caused by radial microfracturing ([25], [30], [43]). At higher temperatures (from 700 °C), in particular in the presence of limestone aggregates (see [36]), the complete breakdown of concrete occurs; it is caused by reactions of de-carbonation and related volumetric expansion. In this situation, aggregates dilate, burst and tend to be pulverised.

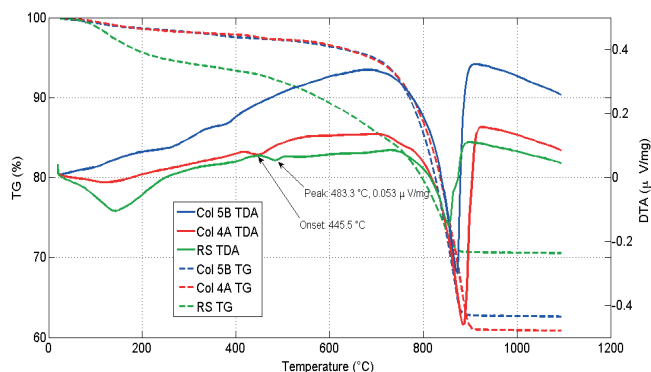


Fig. 24 Multi-plot of TG-DTA curves of selected samples (COL 5B, COL 4A (Sp a) and RS, see Table 9).

Table 10 reports some important diagnostic features of fire-affected concrete, determined by XRD and TG-DTA. This table also shows changes in mechanical strength at different temperature ranges. X-Ray diffraction patterns of the most highly-altered samples consist of calcite and dolomite. Calcite, dolomite, portlandite, ettringite and anhydrous calcium silicates and calcium aluminates were recognised in the RS sample.

The absence of portlandite indicates severe thermal degradation of concrete. A multiplot of selected TG-DTA curves is shown in Figure 24. The thermogram of an RS sample shows an endothermic peak at about 120°C, related to the loss of physically-bound water in hydrated cement constituents (CSH and CAH). At about 500°C, the endothermic peak related to the de-hydroxylation of portlandite was detected. At higher temperatures, the effects of decarbonation of dolomite and calcite begin. A typical thermogram of a sample affected by high thermal decay (e.g. COL 5 B) shows only the endothermic peak (at about 880°C), due to the decarbonation reaction. In other samples (e.g. COL 4A Sp a), the endothermic peak of de-hydroxylation of portlandite (P*) occurs at lower temperatures.

According to some authors, see [42], a significant decrease in de-hydroxylation onset temperature of portlandite occurs in thermally-altered samples.

Therefore, the portlandite (P*) detected in some fired samples could be relict or secondary. Consequently, exposure temperatures which locally affected the concrete could be considered higher than those related to the theoretical de-hydroxylation temperature (see Table 10).

Table 10 Summary of diagnostic features and strength changes in concrete caused by heating (see [25], [28], [30], [31]).

T[°C]	Diagnostic features	Strength Changes
70-80	Dissociation of ettringite, leading to the disappearance of small spines which develop in air bubbles during hydration. Visible under PPTL and SEM.	
>105	The loss of physically-bound water in aggregate and cement paste causes an increase in microcracking and capillary porosity of the cement paste. Endothermic peak at about 115°C. Water loss from CSH gels. Endothermic effect rarely perfectly discriminable starting at about 120 °C.	Minor loss of strength possible (<10%)
120-175	Dissociation of gypsum, causing its depletion in the cement paste. Dehydroxylation of gypsum with formation of alpha hemihydrate at 163 °C.	
235	Water loss from calcium carboalluminates. Endothermic peak at about 175°C	
235	Water loss from hydrate tetracalcic alluminate. Endothermic peak at 235 °C	
>300	Marked increase in porosity and microcracking. Loss of bound water in cement matrix and associated degradation become more prominent. Dehydroxylation of brucite Mg(OH)2. Endothermic peak at about 388°C.	Significant loss of strength starts at 300°C
300-350	Oxidation of FeO-OH to α-Fe2O3: change in colour to pink or reddish brown and disconnection of sand particles.	
573	5% increase in volume of quartz (from phase α to β transition) causing radial cracking around quartz grains in the aggregate. Endothermic peak at about 491°C	
450-500	Dehydroxylation of Portlandite, causing its depletion in the cement paste. Endothermic peak at about 491°C	Decisive reduction of concrete strength for heating at temperatures beyond of 500-600°C
600-800	Release of carbon dioxide from carbonates may cause considerable contraction of the concrete (with severe microcracking of the cement matrix). Early decarbonation of dolomite, first step: 750°-800°C (I)	
800-1200	Decarbonation of dolomite, second step: 850°-950°C (II). Decarbonation of calcite, endothermic peak at about 895°C. Dissociation and extreme thermal stress cause complete disintegration of calcareous constituents, resulting in whitish-grey concrete colour and severe microcracking. Concrete starts to melt at about 1200°C	

Another technique for monitoring changes produced by fire exposure is colorimetry (see [31], [36], [37], [38]), which allows to highlight the colour changes in the concrete. These variations are related to the nature of the concrete and in particular to the nature of the aggregates (see [36]). In this work also this approach has been developed. Some benchmark elements can be useful in this analysis: the literature ([25], [31], [44] for example) reports a reddening of minerals containing iron in the 300–350 °C range due to their oxidation to Fe + 3. Even the cement matrix undergoes slight clearing at these temperatures. Certainly the most obvious is the general lightening of aggregates and the cement matrix at approximately 600°C, with a dark grey colour of the latter in the 600–900°C range, until the browning of the cement matrix between 900°–1000°C. These chromatic changes are strictly dependent on the presence of siliceous or limestone aggregates, the nature of the cementitious binder and exposure time at maximum temperature. To calibrate the colorimetric analysis, measurements on samples collected in situ were compared with the ones obtained from artificially-heated samples. Therefore, 3 cm thick slices were cut from the RS sample, lapped by means of SiC abrasive 200 grit paper and heated in a programmable electric oven (mod. Nabertherm LHT/0216). A thermal gradient of 10°C /min was carried out as treatment up to 400°C; a slower gradient of 5°C /min was used for treatment up to 800°C. Treatment temperatures were increased every 100°C, for every cycle, until the final temperature (800°C). Samples were kept at the targeted conditions for 1 hour. Then samples were slowly cooled, keeping them in the oven. Colorimetric measurements, before and after thermal treatment (TT), were carried out at selected points in the concrete slices (see Figure 25).

Some measurements were performed on the cement matrix (CM); others were carried out on conglomeratic aggregates selected according to their original colours: dark grey, dark brown, light beige, pinkish-beige and ivory.

Spectral power distribution (SPD) is a characteristic of materials and represents the ability of an opaque surface to reflect incoming light at any wavelength in the visible range. SPD can be expressed by a continuous plot that cannot be formulated in a compact form. In addition, the measurement of colours as they are seen by the human eye can be represented by just three numbers, rather than a continuous plot. For these reasons, the International Commission on Illumination (CIE) converted the SPD into just three components CIE XYZ. Any colour can be expressed by a linear combination of these three parameters. Subsequently, in 1976, the CIE proposed the CIE Lab color space (L^* , a^* , b^*). The transformation from CIE XYZ to CIE Lab is performed with the following Eqns (4)–(6) (see [31]):

$$L^* = 116(Y/Y_n)^{1/3} - 16, \quad (4)$$

$$a^* = 500 \left[\left(\frac{X}{X_n} \right)^{1/3} - \left(\frac{Y}{Y_n} \right)^{1/3} \right] \quad (5)$$

$$a^* = 200 \left[\left(\frac{Y}{Y_n} \right)^{1/3} - \left(\frac{Z}{Z_n} \right)^{1/3} \right], \quad (6)$$

where X_n , Y_n , Z_n are the CIE XYZ components for reference white points. Figure 26 shows cement matrix colorimetric average values (L^* , a^* , b^*) during different thermal treatments. Two significant increases in the values of a^* and b^* were observed: one in the temperature range between 300–400°C and one above 700°C. A significant increase starting from 700°C in L^* values was also measured; at this temperature, a general clearing of the concrete is noted (see Figure 25). Measurements of a^* and b^* performed on aggregates (see Figures 27) show a fluctuating trend or a slight decrease up to 200°C. Starting from this temperature, values increased, reaching their maximum at 400°C. A decrease in a^* and b^* values occurred at about 600°C–650°C. Starting from this temperature, their values increased again until the final temperature (800°C). L^* values tended to gradually increase during thermal cycles. A considerable increase was measured starting from 600°C.

3.7 Temperature Assessment

In Table 11, colorimetric measurements of samples collected in situ at different depths were reported. For temperature assessment, two colorimetric targets were selected: colour change in the cement matrix (CM) and redness of originally pinkish-beige aggregates (PBA).

Table 11 also reports the mineralogical phases detected by X-Ray diffraction and TG-DTA techniques. The absence of portlandite (P) indicates that the temperature exceeded 500 °C.

Analysis of the data collected (colorimetric, diffractometric and thermodifferential) shows how various high temperatures were reached in different points/samples of the industrial warehouse (e.g. COL 4, COL 5, BEAM 3, BEAMS 8–9, BEAMS 8–9 a). Considering sample COL 4A Sp a, for example, temperatures probably reached 700 °C in the cortical portion of the concrete (about 0.5–1.5 cm) due to strong clearing of concrete and the presence of portlandite P* (relict or secondary). At greater depths (about 2–3 cm) in the same sample, portlandite (P) was detected: temperature did not exceed 500 °C. About 4–7 cm from the surface, redness systematically appeared in aggregates that had originally been pink-beige. For the other samples, these reddish aggregates were found at variable depths but generally not more than about 8–12 cm deep.

Table 11 Max. temperature estimation, Colorimetric results (L^* , a^* and b^*) and mineralogical phases detected on samples collected in situ. Legend: Cal = Calcite, Dol = Dolomite, P = Portlandite, Ank = Ankerite, Per = Perovskite, Spu = Spurrite, E = Ettringite, P* = relict or secondary Portlandite. CM = Cement Matrix, PBA = Pinkish-beige aggregates. The mark * on the sample label indicates that the original surface was already eroded at the time of drilling.

Sample Labels	Mineralogical phases	Estimated T (°C)	Depth from the top surface (cm)	L^* ; a^* ; b^*	Col. targets
Reference (RS)	E, Cal, Dol, P	20	0,0	62.08; 0.03; 2.72	CM
COL 4A Sp a	Cal, Dol, P*	≈700	0.5	75.35; -0.61; 5.25	CM
COL 4A Sp b	Cal, Dol	> 500	1.5	73.45; 0.27; 4.01	CM
COL 4A Sp c	Cal, Dol, P	≤ 500	2.5	61.23; 0.47; 4.35	CM
COL 4A Sp d	Cal, Dol, P	< 500÷400	4.5	58.36; 3.67; 5.18	PBA
COL 4A Sp e	Cal, Dol, P	400÷300	7.5	54.63; 5.28; 6.43	PBA
COL 5 A*	Cal, Dol, P	≤ 500	6.0	61.84; 0.85; 4.35	CM
COL 5 A*	Cal, Dol, P	400÷300	8.0	55.49; 5.26; 6.25	PBA
COL 5 B	Cal, Dol	> 500	0.5	70.55; 0.21; 4.25	CM
COL 5 B	Cal, Dol, P	≤ 500÷400	2.0	61.78; 0.86; 3.58	CM
COL 5 B	Cal, Dol, P	400÷300	2.7÷4.5	55.49; 5.13; 6.43	PBA
COL 8 A*	Cal, Dol, P	≤500	3.0	61.45; 0.98; 4.74	CM.
COL 8 A	Cal, Dol, P	400÷300	5.0	57.54; 5.36; 6.42	PBA
COL 8 B	Cal, Dol, P	400÷300	0.5	55.49; 5.80; 6.62	PBA
COL 9 A*	Cal, Dol, P	400÷300	9.7	57.40; 4.25; 6.47	PBA
COL 9 B*	Cal, Dol, P	400÷300	7.8	55.12; 4.84; 5.98	PBA
Beam 3	Cal, Dol, Per, Spu	> 500	0.5	70.45; -0.31; 5.83	CM
Beam 3	Cal, Dol, P	≤ 500÷400	1.5	63.12; 1.55; 4.25	PBA
Beam 3	Cal, Dol, P	400÷300	3.5	65.02; 4.28; 6.82	PBA
Beams 8-9	Cal, Dol	> 500	0.3	70.91; 0.12; 4.45	CM
Beams 8-9	Cal, Dol, P	≤ 500÷400	1.2	62.31; 1.15; 3.81	CM
Beams 8-9	Cal, Dol, P	400÷300	2.8	60.32; 4.85; 5.94	PBA
Beams 8-9 (a)*	Cal, Dol	> 500	1.5	70.45; -0.15; 4.74	CM
Beams 8-9 (a)	Cal, Dol, P	≤500÷400	4.0	62.24; 3.95; 6.27	PBA

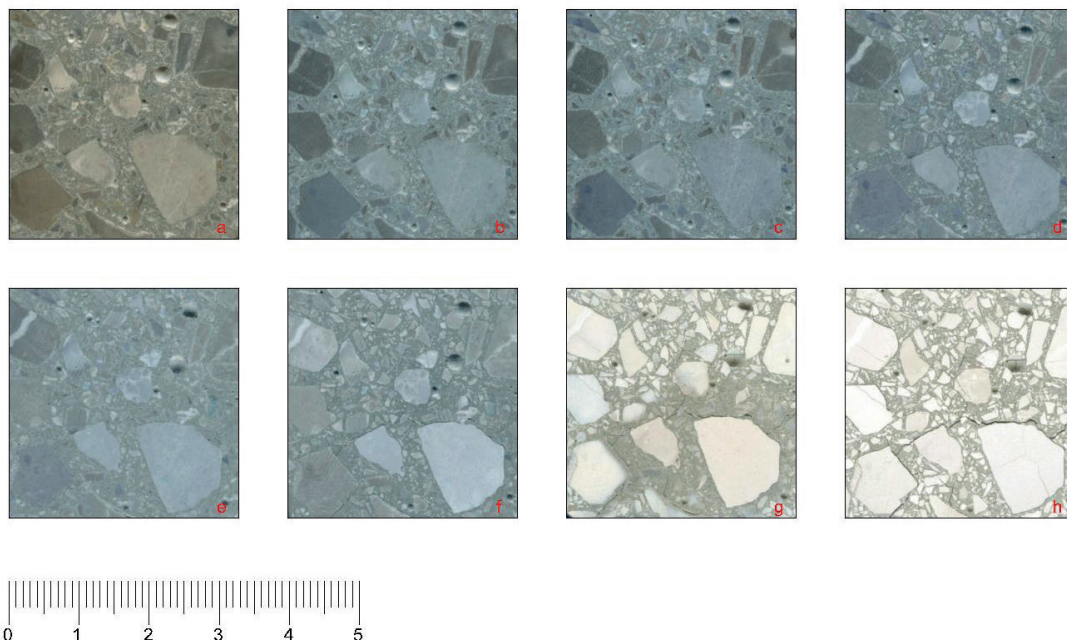


Fig. 25 Concrete slabs before and after thermal treatment; (a) untreated; (b) TT 200°C; (c) TT 300°C; (d) TT 400°C; (e) TT 500°C; (f) TT 600°C; (g) TT 700°C; (h) TT 800°C. The bottom-left scale is in cm.

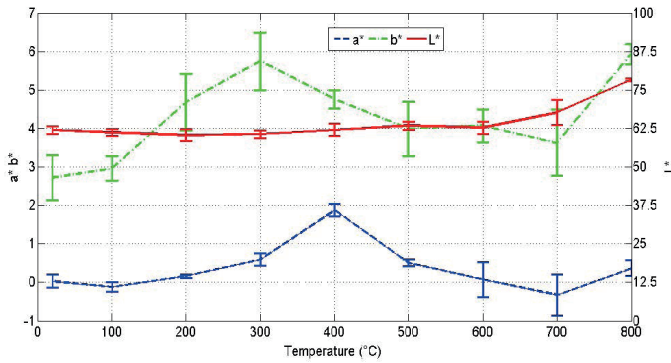


Fig. 26 Average values of L^* , a^* and b^* vs temperature (cement matrix of the RS sample). The error bars represent the standard deviation for each measure..

4 Conclusions

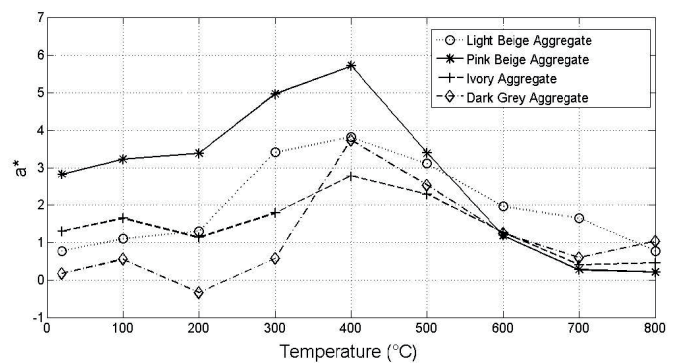
Structural assessment of RC structures after a fire can be a very difficult task. In this paper, several assessment methods (experimental non-destructive and destructive techniques) were applied to a real prestressed R.C. structure damaged by fire in order to present a new integrated approach.

The authors firstly developed a thorough geometric survey by means of laser scanner in order to detect permanent deformations due to fire; then ultrasound wave velocity and rebound index were detected in several elements. In addition, a load test was performed on one of the most representative parts of the damaged structure. Several cylindrical cores were extracted from columns and slabs in different parts of the building. Destructive compressive strength tests were performed on these cores, showing that precast damaged concrete (beams and columns), average strength is 30.5 N/mm^2 , while the compressive strength of cast-on-site damaged concrete (slab) was rated close to 20.0 N/mm^2 .

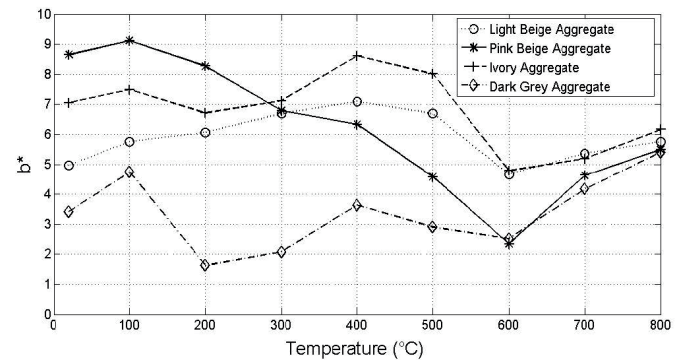
XRD, TG-DTA, OM and SEM, along with colorimetric investigations, have provided useful indications regarding the temperatures reached by the fire-exposed concrete, based on changes in mineralogical composition and microstructure. Portlandite plays a key role in determining the temperatures reached. The absence of this phase reveals reaching of its dehydroxylation temperature at approximately 500°C . The lowering of the dehydroxylation temperature of portlandite can be interpreted as an indicative factor for the presence of relict or secondary portlandite.

Data emerging from the colorimetric study were useful to characterise fire exposure. In detail, concrete strength is dramatically reduced if it has been exposed to heating temperatures beyond $500\text{--}600^\circ\text{C}$. A controlled thermal decaying process on reference concrete provided an accurate definition of the chromatic changes occurring at definite temperature ranges.

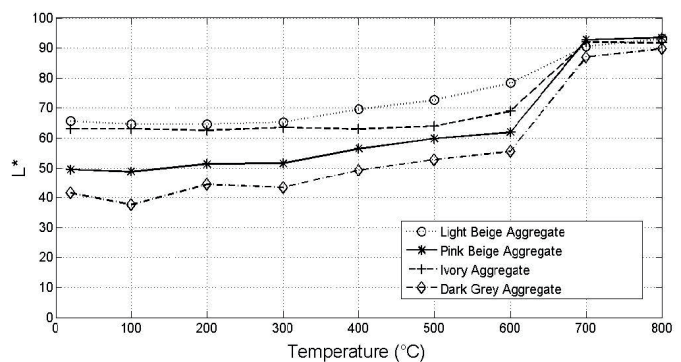
In particular, the reddening of original pinkish-beige aggregates in the $300\text{--}400^\circ\text{C}$ range and the considerable lightening of concrete starting from approximately 700°C are the most relevant changes connected with temperatures.



(a)



(b)



(c)

Fig. 27 Average values of L^* , a^* and b^* vs temperature (aggregates in the RS sample).

The set of integrated data obtained from this study permits recognition of the thermal zoning of fire-exposed concrete that will optimise the restoration of the structure. In particular, the scrapping of surfaces has to include the depth of the concrete at which reddish aggregates emerge. Probably the fire was limited to the central area of the warehouse due to the presence of fire-protected masonry and the first floor slab. Columns 4,5 and 7 displayed the most important damage, and several beams presented important deflections (L1, L4 for example) and have lost the prestressing actions of the tendons. Maximum slab deflection highlighted the deformations of beam T5 and suggests a synthetic map of damages.

Refurbishment is needed, but the structure actually withstood the fire very well. Indeed, the compressive strength and SonReb test certified the quality of the precast concrete and its very good mechanical characteristics. In addition, the load test proved the residual structural safety of the structure.

The field data and the integrated approach presented in this paper, can represent a benchmark for post-fire investigations. Further developments in this research are expected from the numerical models of the structure and the fire scenarios. The information obtained from these models will be of paramount importance for the structural renovation of the building and can help in developing simplified design approach. Indeed, given the complexity of this structural problem, some simplified methods which account for fire loading in an effective way are very helpful for the designer: [45] is an interesting example.

References

- [1] Behnam, B., Ronagh, H. "An Engineering Solution to Improve Post-Earthquake Fire Resistance in Important Reinforced Concrete Structures". *Advances in Structural Engineering*, 17(7), pp. 993–1010. 2014. <https://doi.org/10.1260/1369-4332.17.7.993>
- [2] Shi, J., Shi, W., Ren, A. "An Integrated Model for the Fire Safety Analysis of Large Space Buildings". *Advances in Structural Engineering*, 14(5), pp. 763–776. 2011. <https://doi.org/http://dx.doi.org/10.1260%2F1369-4332.14.5.763>
- [3] Salter, C., Ramachandran, G., Emmitt, N., Bouchlaghem, N. "Economic cost of fire: Exploring UK fire incident data to develop a design tool". *Fire Safety Journal*, 62, pp. 256–263. 2013. <https://doi.org/10.1016/j.firesaf.2013.09.018>
- [4] Fehérvári, S., Nehme, S.G. "Effect of the concrete's component on the heat shock bearing capacity of tunnel linings". *Periodica Polytechnica Civil Engineering*, 53(1), pp. 15–23. 2009. <https://doi.org/10.3311/pp.ci.2009-1.03>
- [5] Bogárdi, I., Fülöp, R. "A Spatial probabilistic model of pipeline failures". *Periodica Polytechnica Civil Engineering*, 55(2), pp. 161–168. 2011. <https://doi.org/10.3311/pp.ci.2011-2.08>
- [6] Giovino, G., Olmati, P., Garbati, S., Bontempi, F. "Blast resistance assessment of concrete wall panels: experimental and numerical investigations". *International Journal of Protective Structures*, 5(3), 349–366. 2014. <https://doi.org/10.1260/2041-4196.5.3.349>
- [7] Acito, M., Stochino, F., Tattoni, S. "Structural response and reliability analysis of RC beam subjected to explosive loading". *Applied Mechanics and Materials*, 82, pp. 434–439. 2011. <https://doi.org/10.4028/www.scientific.net/AMM.82.434>
- [8] Stochino, F. "RC beams under blast load: Reliability and sensitivity analysis". *Engineering Failure Analysis*, 66, pp. 544–565. 2016. <https://doi.org/10.1016/j.engfailanal.2016.05.003>
- [9] Kakogiannis, D., Pascualena, F., Reymen, B., Pyl, L., Ndambi, J.M., Segers, E., Lecompte, D., Vantomme, J., Krauthammer, T. "Blast performance of reinforced concrete hollow core slabs in combination with fire: Numerical and experimental assessment". *Fire Safety Journal*, 57, pp. 69–82. 2013. <https://doi.org/10.1016/j.firesaf.2012.10.027>
- [10] Dadashzadeh, M., Khan, F., Hawboldt, K., Amyotte, P. "An integrated approach for fire and explosion consequence modelling". *Fire Safety Journal*, 61, pp. 324–337. 2013. <https://doi.org/10.1016/j.firesaf.2013.09.015>
- [11] Folic, R., Radonjanin, V., Malesev, M. "The assessment of the structure of Novi Sad Open University damaged in a fire". *Construction and Building Materials*, 16(7), pp. 427–440. 2002. [https://doi.org/10.1016/S0950-0618\(02\)00045-4](https://doi.org/10.1016/S0950-0618(02)00045-4)
- [12] Fletcher, I.A., Borg, N., Hitchen, S., Welch, S. "Performance of concrete in fire: a review of the state of the art, with a case study of the Windsor Tower fire" In: *Proceedings of the 4th International Workshop in Structures in Fire*, Aveiro, Portugal, 2006. pp. 779–790.
- [13] Majoros, E., Balázs, G.L. "Degree of deterioration due to fire in large concrete halls". *Periodica Polytechnica Civil Engineering*, 48(1–2), pp. 141–156. 2004.
- [14] Kose, M., Temiz, H., Binici, H. "Effects of fire on precast members: A case study". *Engineering Failure Analysis*, 34(6), pp. 1001–1005. 2004. <https://doi.org/10.1016/j.engfailanal.2005.12.003>
- [15] Tattoni, S., Stochino, F. "Collapse of prestressed reinforced concrete jetties: durability and faults analysis". *Case Studies in Engineering Failure Analysis*, 1(2), pp. 131–138. 2013. <https://doi.org/10.1016/j.csefa.2013.05.006>
- [16] Xiao, J., König, G. "Study on concrete at high temperature in China—an overview". *Fire Safety Journal*, 39(1), pp. 89–103. 2004. [https://doi.org/10.1016/S0379-7112\(03\)00093-6](https://doi.org/10.1016/S0379-7112(03)00093-6)
- [17] Lamont, S., Lane, B., Graeme, F., Usmani, A. "Behaviour of Structures in Fire and Real Design – A Case Study". *Journal of Fire Protection Engineering*, 16(1), pp. 5–35. 2006. <https://doi.org/10.1177/1042391506054038>
- [18] Tang, P., Huber, D., Akinci, B., Lipman, R., Lytle, A. "Automatic reconstruction of as-built building information models from laser-scanned point clouds: A review of related techniques". *Automation in Construction*, 19(7), pp. 829–843. 2010. <https://doi.org/10.1016/j.autcon.2010.06.007>
- [19] Vacca, G., Mistretta, F., Stochino, F., Dessi, A. "Terrestrial Laser Scanner for Monitoring the Deformations and the Damages of Buildings". *ISPRS-International Archives of the Photogrammetry, Remote Sensing and Spatial Information Sciences*, 41, pp. 453–460. 2016. <https://doi.org/10.5194/isprsarchives-XLI-B5-453-2016>
- [20] Li, M., Qian, C.X., Sun, W. "Mechanical properties of high-strength concrete after fire". *Cement and Concrete Research*, 34(6), pp. 1001–1005. 2004. <https://doi.org/10.1016/j.cemconres.2003.11.007>
- [21] Cioni, P., Croce, P., Salvatore, W. "Assessing fire damage to R.C. elements". *Fire Safety Journal*, 36(2), pp. 181–199. 2001. [https://doi.org/10.1016/S0379-7112\(00\)00050-3](https://doi.org/10.1016/S0379-7112(00)00050-3)
- [22] Colombo, M., Felicetti, R. "New NDT techniques for the assessment of fire-damaged concrete structures". *Fire Safety Journal*, 42(6–7), pp. 461–472. 2007. <https://doi.org/10.1016/j.firesaf.2006.09.002>
- [23] Lin, Y., Hsiao, C., Yang, H., Lin, Y.F. "The effect of post-fire-curing on strength–velocity relationship for nondestructive assessment of fire-damaged concrete strength". *Fire Safety Journal*, 46(4), pp. 178–185. 2011. <https://doi.org/10.1016/j.firesaf.2011.01.006>
- [24] Raju, S., Dharmar, B. "Mechanical Properties of Concrete with Copper Slag and Fly Ash by DT and NDT". *Periodica Polytechnica Civil Engineering*, 60(3), pp. 313–322. 2016. <https://doi.org/10.3311/PPci.7904>
- [25] Annerel, E., Taerwe, L. "Revealing the temperature history in concrete after fire exposure by microscopic analysis". *Cement and Concrete Research*, 39(12), pp. 1239–1249. 2009. <https://doi.org/10.1016/j.cemconres.2009.08.017>
- [26] Hollis, N.W. "Petrographic Methods of Examining Hardened Concrete: A Petrographic Manual". Technical report VTRC-92-R14, Virginia Transportation Research Council (VTRC), 1992.
- [27] Nijland, T.G., Larbi, J.A. "Unravelling the temperature distribution in fire-damaged concrete by means of PFM microscopy: Outline of the approach and review of potentially useful reactions". *Heron*, 46(4), pp. 253–264. 2001.
- [28] Georgali, B., Tsakiridis, P.E. "Microstructure of fire-damaged concrete. A case study". *Cement and Concrete Composite*, 27(2), pp. 255–259. 2005. <https://doi.org/10.1016/j.cemconcomp.2004.02.022>

- [29] Orioz, O. "Effects of elevated temperatures on properties of concrete". *Fire Safety Journal*, 42(8), pp. 516–522. 2007. <https://doi.org/10.1016/j.firesaf.2007.01.003>
- [30] Ingham, J. P. "Application of petrographic examination techniques to the assessment of fire-damaged concrete and masonry structures". *Materials Characterization*, 60(7), pp. 700–709. 2009. <https://doi.org/10.1016/j.matchar.2008.11.003>
- [31] Annerel, E., Taerwe, L. "Methods to quantify the colour development of concrete exposed to fire". *Construction and Building Materials*, 25(10), pp. 3989–3997. 2011. <https://doi.org/10.1016/j.conbuildmat.2011.04.033>
- [32] Alarcon-Ruiz, L., Plateret, G., Massieu, E., Ehrlacher, A. "The use of thermal analysis in assessing the effect of temperature on a cement paste". *Cement and Concrete Research*, 35(3), pp. 609–613. 2005. <https://doi.org/10.1016/j.cemconres.2004.06.015>
- [33] Mindeguia, J. C., Pimienta, P., Noumowé, A., Kanema, M. "Temperature, pore pressure and mass variation of concrete subjected to high temperature - Experimental and numerical discussion on spalling risk". *Cement and Concrete Research*, 40(3), pp. 477–487. 2010. <https://doi.org/10.1016/j.cemconres.2009.10.011>
- [34] Ramachandran, V.S., Beaudoin, J.J. "Handbook Of Analytical Techniques In Concrete Science And Technology, Principles, Techniques, and Applications." Noyes Publications / William Andrew Publishing, LLC Norwich, New York, NY. 2001.
- [35] Taylor, H.F.W., Beaudoin, J.J. "The Chemistry of Cements." Academic Press Inc., London, UK. 1964.
- [36] Xing, Z., Beaucour, A.L., Hebert, R., Noumowe, A., Ledesert, B. "Influence of the nature of aggregates on the behaviour of concrete subjected to elevated temperature". *Cement and Concrete Research*, 41(4), pp. 392–402. 2011. <https://doi.org/10.1016/j.cemconres.2011.01.005>
- [37] Breysse, D. "Nondestructive evaluation of concrete strength: An historical review and a new perspective by combining NDT methods". *Construction and Building Materials*, 33, pp. 139–163. 2012. <https://doi.org/10.1016/j.conbuildmat.2011.12.103>
- [38] Felicetti, R. "Digital camera colorimetry for the assessment of fire-damaged concrete" In: Proceedings of the Workshop: Fire Design of Concrete Structures: What now? What next?, Milan, Italy, 2004. pp 211–220.
- [39] UNI EN 13501-1:2009. "Fire classification of construction products and building elements - Part 1: Classification using data from reaction to fire tests", 2009.
- [40] Concu, G., De Nicolo, B., Pani, L., Trulli, N., Valdés M. "Prediction of Concrete Compressive Strength by Means of Combined non-destructive Testing". *Advanced Materials Research*, 894. pp. 77–81, 2014. <https://doi.org/10.4028/www.scientific.net/AMR.894.77>
- [41] Concu, G., B. De Nicolo, L. Pani "Non-destructive testing as a tool in reinforced concrete buildings refurbishments". *Structural Survey*, 29(2), pp. 147–161. 2011. <https://doi.org/10.1108/02630801111132821>
- [42] Fiore, A., Porco, F., Uva, G., Mezzina, M. "On the dispersion of data collected by in situ diagnostic of the existing concrete". *Construction and Building Materials*, 47, pp. 208–217. 2013. <https://doi.org/10.1016/j.conbuildmat.2013.05.001>
- [43] Matesova, D., Bonen, D., Shah, S.P. "Factors affecting the resistance of cementitious materials at high temperatures and medium [0] heating rates". *Materials and Structures*, 39, pp. 455–469. 2006. <https://doi.org/10.1007/s11527-005-9041-4>
- [44] Short, N.R., Purkiss, J.A., Guise, S.E. "Assessment of fire-damaged concrete using colour image analysis". *Construction and Building Materials*, 15(1), pp. 9–15. 2001. [https://doi.org/10.1016/S0950-0618\(00\)00065-9](https://doi.org/10.1016/S0950-0618(00)00065-9)
- [45] Tattoni, S., Stochino, F., Caldara, F. "A simplified approach to serviceability assessment of reinforced concrete structures in fire" In: Proceedings of 14th International Conference on Civil, Structural and Environmental Engineering Computing, Cagliari, Italy. Civil-Comp press, CCP: 102. 2013. <https://doi.org/10.4203/ccp.102.120>